NAVAL
POSTGRADUATE
SCHOOL

MONTEREY, CALIFORNIA

THESIS

ATMOSPHERIC EFFECTS ON RADIO FREQUENCY (RF) WAVE PROPAGATION IN A HUMID, NEAR-SURFACE ENVIRONMENT

by

Samuel P. Mason

March 2010

Thesis Co-Advisors:	Peter S. Guest Andreas K. Goroch

REPORT DOCUMENTATION PAGE

Form Approved OMB No. 0704-0188

1. AGENCY USE ONLY *(Leave blank)*

2. REPORT DATE March 2010

3. REPORT TYPE AND DATES COVERED Master's Thesis

4. TITLE AND SUBTITLE: Atmospheric Effects on Radio Frequency (RF) Wave Propagation in a Humid, Near-Surface Environment

5. FUNDING NUMBERS

6. AUTHOR(S) Samuel P. Mason

7. PERFORMING ORGANIZATION NAME(S) AND ADDRESS(ES)
Naval Postgraduate School
Monterey, CA 93943-5000

8. PERFORMING ORGANIZATION REPORT NUMBER

9. SPONSORING /MONITORING AGENCY NAME(S) AND ADDRESS(ES)
N/A

10. SPONSORING/MONITORING AGENCY REPORT NUMBER

11. SUPPLEMENTARY NOTES The views expressed in this thesis are those of the author and do not reflect the official policy or position of the Department of Defense or the U.S. Government. IRB Protocol number ________________.

12a. DISTRIBUTION / AVAILABILITY STATEMENT
Approved for public release; distribution is unlimited

12b. DISTRIBUTION CODE A

13. ABSTRACT (maximum 200 words)

Currently, the meteorological and physical phenomena associated with the various dynamic processes in the very near surface environment (for example, within the surface layer), are poorly understood. By properly characterizing what is happening in the real world, there is potential for obtaining an empirical formula that correlates well with real world data, and thus can be used as a means of quantifying these physical processes. This, in turn, can be used to more accurately model the effects of the atmosphere on RF waves. This thesis is an analysis of the propagation loss measurements taken from the Near Earth Propagation-6 (NEP-6), Panama City, FL, experiment in Aug 2009, where propagation loss was measured at 1768 MHz within a few wavelengths (≈ 0.5 meters) of the surface. The results support and extend the near-surface, short range RF propagation conclusions drawn by Merrill et al. (2004). In particular, we focus on a novel technique that takes advantage of tidal sea level variation to continuously vary antenna height above the surface. Results confirm a strong dependence of propagation loss on antenna height similar to Merrill et al.'s (2004) observations.

14. SUBJECT TERMS: Electromagnetic propagation, electromagnetic scattering, Ground-wave propagation, Mathematical techniques, Variance reduction.

15. NUMBER OF PAGES 87

16. PRICE CODE

17. SECURITY CLASSIFICATION OF REPORT	**18. SECURITY CLASSIFICATION OF THIS PAGE**	**19. SECURITY CLASSIFICATION OF ABSTRACT**	**20. LIMITATION OF ABSTRACT**
Unclassified	Unclassified	Unclassified	UU

NSN 7540-01-280-5500

Standard Form 298 (Rev. 2-89)
Prescribed by ANSI Std. 239-18

THIS PAGE INTENTIONALLY LEFT BLANK

ATMOSPHERIC EFFECTS ON RADIO FREQUENCY (RF) WAVE PROPAGATION IN A HUMID, NEAR-SURFACE ENVIRONMENT

Samuel P. Mason
Lieutenant, United States Navy
B.S., United States Naval Academy, 2002

Submitted in partial fulfillment of the
requirements for the degree of

MASTER OF SCIENCE IN METEOROLOGY

from the

NAVAL POSTGRADUATE SCHOOL
March 2010

Author: Samuel P. Mason

Approved by: Peter S. Guest
Co-Advisor

Andreas K. Goroch
Co-Advisor

Phillip Durkee
Chairman, Department of Meteorology

THIS PAGE INTENTIONALLY LEFT BLANK

ABSTRACT

Currently, the meteorological and physical phenomena associated with the various dynamic processes in the very near surface environment (for example, within the surface layer), are poorly understood. By properly characterizing what is happening in the real world, there is potential for obtaining an empirical formula that correlates well with real world data, and thus can be used as a means of quantifying these physical processes. This, in turn, can be used to more accurately model the effects of the atmosphere on RF waves. This thesis is an analysis of the propagation loss measurements taken from the Near Earth Propagation-6 (NEP-6), Panama City, FL, experiment in Aug 2009, where propagation loss was measured at 1768 MHz within a few wavelengths (≈ 0.5 meters) of the surface. The results support and extend the near-surface, short range RF propagation conclusions drawn by Merrill et al. (2004). In particular, we focus on a novel technique that takes advantage of tidal sea level variation to continuously vary antenna height above the surface. Results confirm a strong dependence of propagation loss on antenna height similar to Merrill et al. (2004) observations.

THIS PAGE INTENTIONALLY LEFT BLANK

TABLE OF CONTENTS

LIST OF FIGURES

LIST OF TABLES

THIS PAGE INTENTIONALLY LEFT BLANK

LIST OF ACRONYMS AND ABBREVIATIONS

ABL	Air Boundary Layer
CPU	Central Processing Unit
dB	Decibel
dBm	Decibels referenced to one milliwatt
DC	Direct Current
DoD	Department of Defense
d/dz	Gradient in Height
e	Saturation Vapor Pressure
EM/EO	Electromagnetic/Electro-Optical
GPS	Global Positioning System
IED	Improvised Explosive Device
M	Modified Index of Refraction
n	Index of Refraction
N	Refractivity
NEP-6	Near-Earth Propagation (6th in series)
NOAA	National Oceanic and Atmospheric Administration
NPS	Naval Postgraduate School
NRL	Naval Research Laboratory
NSWC-PC	Naval Surface Warfare Center – Panama City
NTP	Network Time Protocol
PMCC	Pearson Product-Moment Correlation
PVC	Polyvinyl Chloride
q	Specific Humidity
RF	Radio Frequency
RH	Relative Humidity
RSSI	Received Signal Strength Indication
ρ	Air density
T	Temperature

THIS PAGE INTENTIONALLY LEFT BLANK

ACKNOWLEDGMENTS

First and foremost, I would like to thank the Lord for his grace, support and peace. Additionally, this thesis would not have been possible without the guidance and solid support of several individuals. My thanks and sincere gratitude go to Dr. Peter Guest and Dr. Andreas Goroch. These fine gentlemen are exacting scientists and consummate professionals, and it was by their patient guidance, thought provoking ideas, and gentle corrections that this research project came to fruition. Thank you as well to Mr. Dick Lind for his efforts in designing and building the NPS measurement suite, in addition to his daily quips that always brought a smile to my face.

Next, I would like to thank Mr. Robert Wert, Evan Worthington, and Vincent Wong in the Tactical Electronics Warfare Division at Naval Research Laboratory, Washington DC for their organizing the tests and providing advice and support in the collection and analysis of the propagation measurements. It was through them that I learned what field research really was.

Any worthwhile endeavor requires not only intellectual, but also financial support. I would like to thank the NPS JIEDDO foundation for their considerable and ongoing commitment to furthering this area of research and in so doing, making this project feasible.

Finally, I extend my love and appreciation to my dearest wife, whose constant support, gentle understanding, and quiet willingness to simply listen to both my rants of frustration, as well as my giddy declarations of success, were integral in my ability to complete this work.

THIS PAGE INTENTIONALLY LEFT BLANK

I. INTRODUCTION

A. MOTIVATION

Currently, the effects of meteorological and physical phenomena associated with the various dynamic and thermodynamic processes in the very near surface environment (i.e., within the lowest 10% of the surface layer), is poorly understood. By properly characterizing what is happening in the real atmosphere, we can obtain an understanding of the physical processes involved in radio frequency (RF) transmissions, with the goal of obtaining empirical formulas relating these processes. These, in turn can be used to more accurately model RF propagation at short ranges and near the surface. This study is a crucial step to more reliable communications with unmanned vehicles, wireless networks and a more effective means of detecting, jamming, and/or pre-detonating mines and IEDs in various environments.

B. BACKGROUND

1. Electromagnetic Waves

Electromagnetic radiation (EM) consists of alternating electric and magnetic fields (Figure 1). The electric field vector is perpendicular to the magnetic field vector, and the direction of propagation is perpendicular to both. The fundamental unit of frequency, ν, is the hertz (Hz), rather one cycle per second and is related to wavelength λ, by

$$\nu = {}^{c}\!/\!_{\lambda}, \tag{1}$$

Where, c is the speed with which electromagnetic radiation travels in a vacuum (2.997 x 10^8 m s-1) and is known as the speed of light. In the atmosphere, it travels slightly more slowly due to interaction with air molecules.

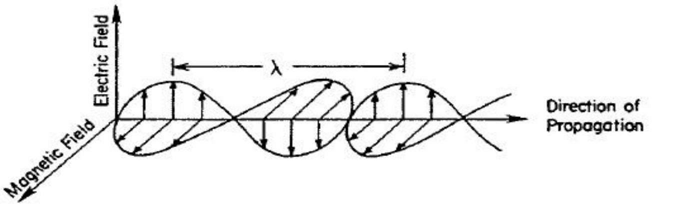

Figure 1. Schematic representation of EM waves (From Kidder and Vonder Haar et al. [and elsewhere], 1995).

The standard description of a plane wave electric field is

$$E(k,R) = A\frac{e^{ikR}}{kR} \tag{2}$$

where k is the wave number ($2\pi/\lambda$) and R is the scalar distance between the transmitted and received signal. The wavelength is related to the frequency by the speed of the signal, which in this case is the speed of light. The power transmitted by the electric field is

$$\begin{aligned} P &= \left|E\right|^2 \\ &= \left|\frac{e^{ikR}}{kR}\right|^2 \end{aligned} \tag{3}$$

Radiation is often specified by its wavelength, λ, which is the distance between crests of the electric or magnetic fields as depicted in Figure 1. The electromagnetic spectrum spans a wide range of wavelengths from the ultraviolet to the microwave region. This thesis focuses on the 1.78 GHz frequency.

2. Atmospheric Effects on Propagation

An EM signal propagating through a medium consisting of atoms and molecules (i.e., not a vacuum), will interact with that medium through various processes, among them absorption and scattering of EM energy. The efficiency of the interaction is related to the amount of signal absorption. Changes in propagation velocity due to this interaction results in a change in the wave's direction, called refraction and is described by its index of refraction (Bean et al., 1966).

It is important to note that only minor changes in refractive index are necessary to cause a significant change in energy propagation. By using the relationship between refractivity (defined below) and refractive index, n can be derived in terms of total pressure, temperature, and water vapor concentration, as shown in Equation (4). Variations of temperature and moisture in the propagation path cause local refraction of the signal, resulting in signal loss and increase of noise (Thayer, 1974).

$$n \;=\; 77.6 \text{ x } 10^{-6} \left(\frac{\mathrm{P}}{\mathrm{T}}\right) \;-\; 5.6 \text{ x } 10^{-6}\left(\frac{e}{T}\right) \;+\; 3.73 \text{ x } 10^{-1} \left(\frac{e}{\mathrm{T}^{2}}\right) \;+\; 1 \qquad (4)$$

where n : index of refraction
T : temperature (°K)
P : localized atmospheric pressure (mbar)
e : water vapor pressure (mbar)

Since $n \approx 1$ in the atmosphere the only portion of this parameter that truly matters is tied to the fourth, fifth and sixth decimal places. To alleviate the use of exceedingly small numbers, scientists have found it useful to define another parameter, called refractivity (N) and is related to n by $(n - 1)$ x 10^6, or similarly:

$$N = 77.6\left(\frac{P}{T}\right) - 5.6\left(\frac{e}{T}\right) + 3.73\times10^{5}\left(\frac{e}{T^{2}}\right) \qquad (5)$$

where N : refractivity
T : temperature (°K)
P : localized atmospheric pressure (mbar)
e : water vapor pressure (mbar)

Note the strong variability due to humidity (vapor pressure). *On average*, refractivity decreases with altitude, but at a gradually decreasing rate (Rinehart, 1997).

It is often more convenient to represent EM radiation as rays of energy instead of waves. Rays are lines along which waves travel and are drawn perpendicular to each wave front. Snell's Law (also known as Descartes' law) is a formula used to describe the relationship between the angles of incidence and refraction of rays passing through a boundary between two different isotropic media:

$$n_1\sin(\theta_1) = n_2\sin(\theta_2), \tag{6}$$

where θ_1, θ_2 are the incoming and outgoing incident angles (respectively), and n_1, n_2 are the indices of refraction of two isotropic materials. These indices of refraction of the media are used to represent the factor by which a wave's speed decreases when traveling through a refractive medium (Medwin, 2000). Snell's law quantifies these speed changes in the form of angular change, rather, the degree of "bending" of the ray. This bending is one component which affects signal strength. Additionally, by knowing the refractive index in the atmosphere at each level, one can predict the path the EM waves will follow (Rinehart, 1997). See Figure 2.

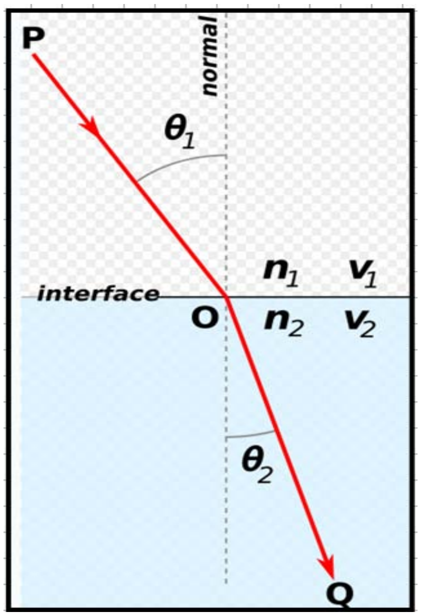

Figure 2. Refraction via Snell's Law, where θ_1/θ_2 are incident and refracted angles (respectively), and n_1/n_2 are the indices of refraction for each medium (Rinehart, 1997).

Finally, scattering of EM radiation also plays a part in the total of atmospheric effects. Scattering is a function of several factors: particle shape, size, index of refraction, wavelength (λ) and viewing geometry. In 1908, Mie applied Maxwell's equations (which describe EM radiation), to the case of a plane electromagnetic wave incident on a sphere. Mie showed that for a spherical scatterer, the scattered radiation is a function of only viewing angle, θ, and the size parameter defined as:

$$\chi \equiv \frac{2\pi r}{\lambda}, \tag{7}$$

where r is the radius of the sphere.

This size parameter can be used to divide scattering into three regimes. Mie scattering occurs for size parameters in the range of 0.1–50 in which the wavelength of the radiation and the circumference of the particle are comparable. Rays undergoing Mie scattering are strongly scattered forward and backward, respectively. For χ greater than about 50, the scatterer is large in comparison to the wavelength of the radiation and results in Geometric optics, widely observed in the occurrence of rainbows following a storm. Geometrically scattered rays are very strongly oriented forward. Finally, Rayleigh scattering results when the size parameter is much smaller than the given wavelength and thus is largely insensitive to particle shape (Kidder et al., 1995). See Figure 3.

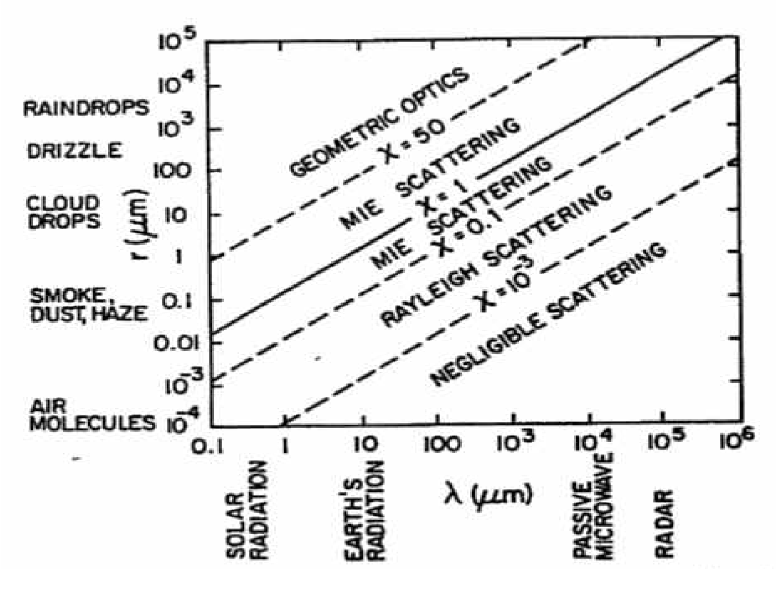

Figure 3. Scattering regimes with respect to wavelength (λ), particle cross-sectional size *r*, and size parameter (χ) (Kidder et al., 1995).

3. Characterization of Water Surface

Regardless of the regime, how RF radiation is reflected or absorbed is a complicated process and approximations are often used in place of rigorous calculations. These approximations of reflectance properties include Lambertian and specular reflectance. Lambertian, also known as isotropic reflectance, occurs when rays are equally reflected in all directions, e.g., fog. Specular, or "mirror-like" reflectance occurs when rays are scattered in a specific direction, such as over a smooth body of water. Depending on the surface material type, index of refraction (*n*), incident angle and roughness, diffuse scattering may also occur (Kidder et al., 1995).

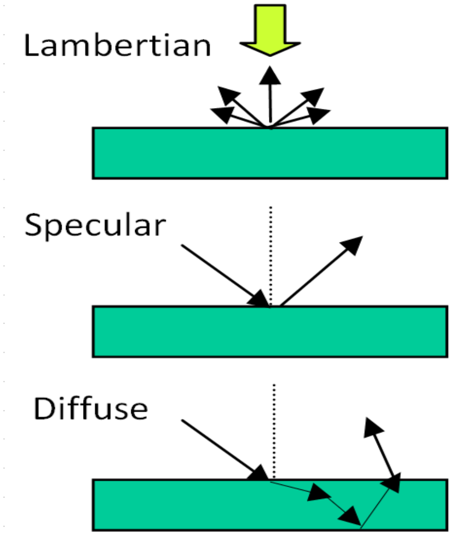

Figure 4. Forms of scattering (After Kidder et al., 1995).

The importance of scattering is quantified by σ_o, the scattering cross section, and is most well known for its use in the radar equation. There are two primary mechanisms which contribute to σ_o, namely specular reflection (as mentioned previously), as well as resonant or Bragg scatter. Surface waves that are near the backscatter radiation length, L_b,

$$L_b = \frac{\lambda}{2\sin(\theta)} \tag{8}$$

when subjected to coherent EM/EO waves greater than 20° off nadir (θ), will be Bragg scattered. This simply means that reflected radiation from one wave reinforces (or cancels) that from the successive wave (Kidder et al., 1995, p. 246).

Another important aspect of the water surface is roughness. Surface roughness occurs when wind induces waves of all wavelengths on the sea surface. Currently, the best indicator available of surface roughness can be found in sea state tables that relate wave height to wind speed. However, it is unlikely that this manner of quantifying surface roughness will play a part in the near surface environment. Other contributors to surface roughness include currents, tides, precipitation and turbulence.

4. Other Factors Affecting Transmission Loss

Ultimately, we seek to link signal propagation loss to the micrometeorology associated with various processes occurring within the near Earth environment. A number of those traditional sources of transmission loss were addressed in the preceding sections. However, there exist other significant propagation mechanisms, and their affects must also be taken into account.

An atmosphere at rest produces no variations in amplitude, phase shift or angle-of-arrival. While this is not the environment in which we work, fortunately, the myriad effects on RF wave propagation in the free atmosphere are well documented. One such affect is attenuation by molecular gaseous absorption; however, it is only noted here, as there is very little molecular absorption of RF energy over short distances.

In contrast to the above, the propagation loss due to the diffusion (spreading) of the EM waves' energy over distance from the source possesses tremendous influence over an RF waves' propagation behavior and strength. The two major geometries utilized to model this spreading effect are spherical, in which intensity (I) is proportional to $\left(\frac{1}{r^2}\right)$ and cylindrical, in which $I \propto \left(\frac{1}{r}\right)$, where r is the radial distance from the source (Medwin, 2000). Since power is the square of intensity, the 4th power drop off is shown in spherical spreading.

Refractive losses, specifically those due to changes in wave propagation speed through a medium, can result in either a loss or a gain of signal strength. Constructive interference results in an increase in signal strength, while destructive interference can reduce or obliterate entirely received signal strength. These effects are due to *multipath*, which is the propagation phenomenon resulting when an RF signal reaches the receiving antenna by two or more paths. Causes of multipath include atmospheric ducting, ionospheric reflection and refraction, and reflection from terrestrial objects, such as mountains, buildings or ocean waves (FS 1037C, 1996). Additionally, the weight of the influence of multipath depends upon frequency, path length (or phase) difference and the reflection coefficient of the reflecting surface. This element was crucial to this thesis and can be best described as the relative "sum" of the direct path and scatter path ray, where signal strength is increased when phase difference is very small (i.e., nearly zero) and wave propagation is reduced when phase difference is large (i.e., maximum destructive interference).

As well as the aforementioned convergence, divergence and multipath effects, waves propagating through a medium comprised of a particular type of gradient can bend downward more than the Earth's curvature and propagate well over the horizons. Dubbed a *trapping layer*, this phenomenon is one of several classes of refractivity. Before investigating these further, one must first be able to clearly identify those regions where this propagation pattern is most likely to occur. When the gradient of N is less than -0.157 m-1, an atmospheric duct can likely be found. Unfortunately, this is rather difficult to ascertain visually from traditional N vs. z diagrams. This problem was solved with the introduction of the modified refractivity parameter, M.

$$M = 77.6\frac{p}{T} - 5.6\frac{e}{T} + 375000\frac{e}{T^2} + 0.157z \tag{9}$$

Where: T is temperature (°K)
p is atmospheric pressure (mbar)
e is partial water vapor pressure (mbar)
z is height above surface (meters)

Modified refractivity is used to determine how rays are bent relative to the Earth's curvature and assist in determining regions of ducting. This is illustrated by way of Figure 5, an adaptation from Helvey et al. (1983), in which the areas of negative gradient contain a high likelihood of a duct. Thus, ducts, which can be surface based or elevated, are simply atmospheric layers that have formed when *M* decreases with height. Radar or other EM waves can be "trapped" within them and may result in greater energy propagation than normally expected.

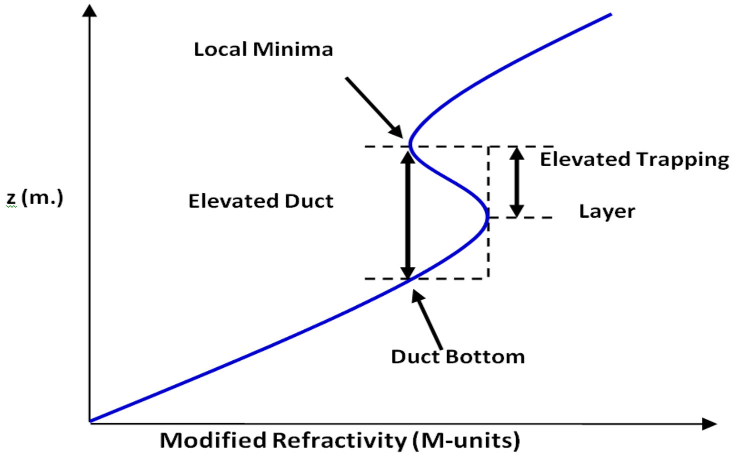

Figure 5. Elevated trapping layer, which enables extended EM wave propagation.

In addition to ducting, EM waves can also be refracted in different ways and their behavior forms the basis of the classes of refractivity. When rays are *sub-refracted*, their propagation distance to the horizon has been decreased and occur when dM/dz > 157 (unitless). Conversely, *super-refracted* rays occur when 78 > dM/dz > 0 and distance to the horizon will increase. Finally, *normal refracted* rays occur for 157 > dM/dz > 78, and distance of propagation is unaffected outside of typical propagation loss terms (see Figure 6)

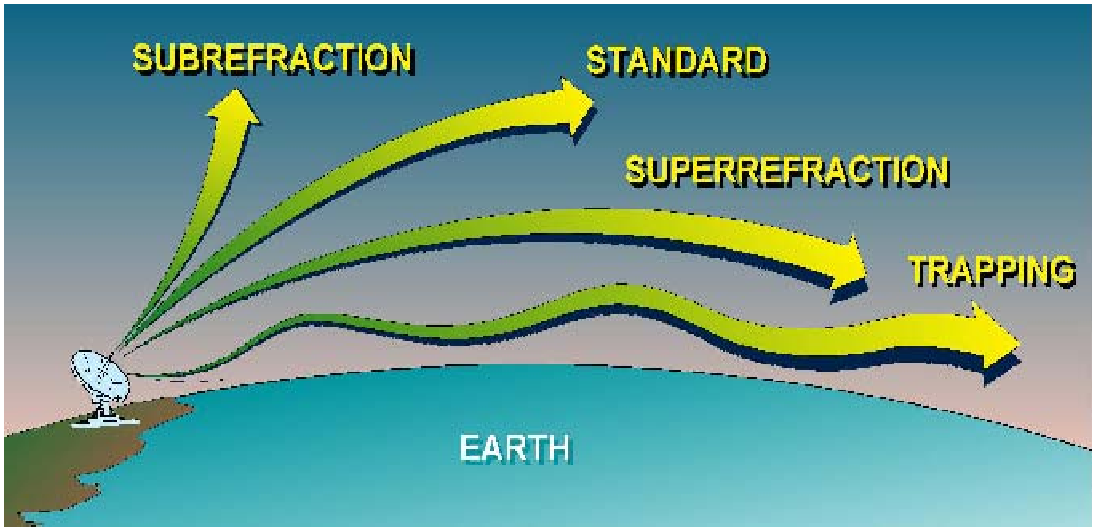

Figure 6. Refraction categories (SPAWAR Systems Center, 2007). Center

II. EXPERIMENT

A. INTRODUCTION

The Panama City Near-Earth Propagation Test (NEP-6) was designed to build upon previous experimentation conducted by Naval Research Laboratories (NRL) under their Near-Earth Propagation (NEP) program. This research effort investigated the unique radio frequency (RF) phenomena that occur within the lowest two to three meters above the Earth's surface. The results of this experiment form the subject of this thesis. The purpose of the NEP-6 was to measure the propagation of radio frequency (RF) signals close to the earth's surface but in an environment characterized by high atmospheric humidity and surfaces of high liquid water content.

While understanding RF effects is certainly worthwhile from a basic scientific standpoint, the underlying reason behind this endeavor is to address a recently identified threat to maritime defense and harbor areas in particular.

B. METHODOLOGY

The NEP-6 program collected meteorological and radio frequency data in the open atmosphere under a variety of environmental conditions. The test was hosted by the Naval Surface Warfare Center in Panama City Beach, FL, with data being collected in two separate segments over a period of time from 21 August 2009 to 02 September 2009. Part one investigated RF propagation over land adjacent to a body of water—in this case, the shore of St. Andrew's Bay. Part two focused on RF wave propagation strictly over a body of water and is the focus of this analysis. Data for this portion were collected from 29 August 2009 until completion of the experiment. The meteorological and RF transmit/receive equipment were situated over a small inlet of the Ovauahannah River, known locally as "Alligator Bayou." The bayou is connected to the Gulf of Mexico and as such water level varies diurnally due to the tides (Figure 7).

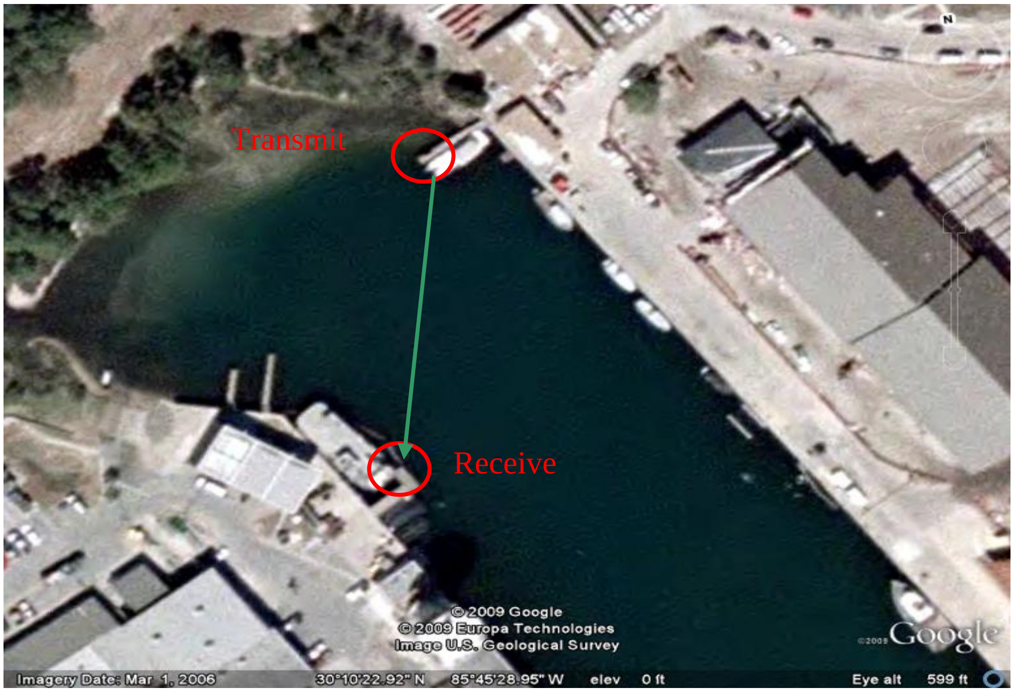

Figure 7. Alligator Bayou, NSWC-PC.

Figure 8. Northern transmit site on floating dock, NSWC-PC.

The signal variation was measured in the 225 MHz, 760 MHz, and 1786 MHz RF spectral regions with omni-directional disc cone and horn transmit and receive antennas placed near the surface of the water. The investigation was comprised of two test sites: a transmit station located to the North on a floating dock (Figure 8), and a receive site placed 73 meters to the South on a permanent (non-floating) dock (Figure 7). Both sites included a full meteorological tower while the transmit site contained additional IR temperature and Campbell water temperature probes, as well as a 3-D sonic anemometer, pyranometer, and LI-COR open path gas analyzer for moisture, temperature and CO_2 flux. Furthermore, a few salinity measurements were obtained manually at both sites. This configuration enabled the collection of data necessary to study the effects of surface roughness, temperature and humidity gradient, turbulence and tidal and salinity variation on changes in the net loss of RF energy.

C. DISTRIBUTED SENSOR SETUP

Over the course of four days, multiple data collection runs were conducted at periods of predominantly twelve and twenty-four hours in length. Individual nodes were established at both the North (Tx) and South (Rx) positions, where each sites' laptop computer collected and time-stamped RF data internally. In addition to the RF data logging, meteorological data were stored on a separate Campbell data logger. All of this information was then synchronized with GPS time using an NTP time server broadcasting over a secure wireless network. Finally, all recorded data were downloaded from the data logger to a master computer on a daily basis. This was done to prevent potential data loss due to failure of the Campbell data logger's flash media cards. Even with these safeguards in place, there were some brief periods of no data collection

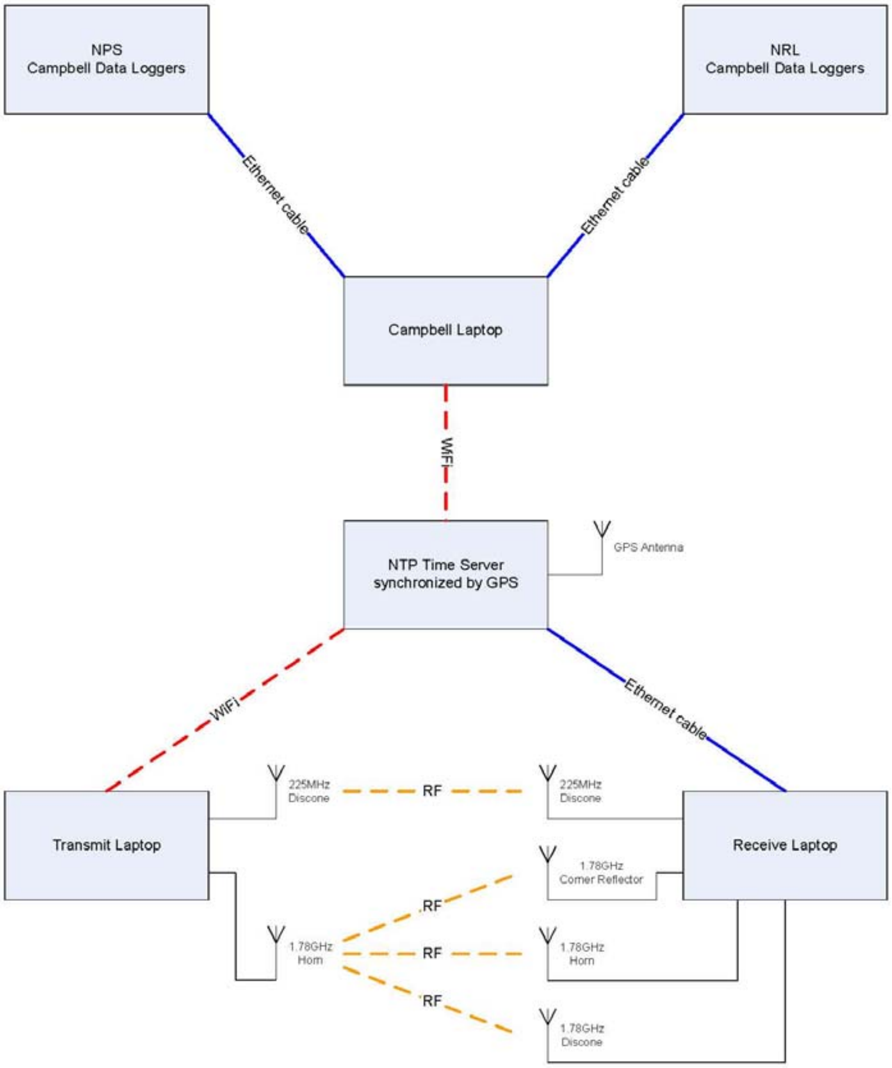

Figure 9. PC layout of data logger network, from Wong (2009).

D. EQUIPMENT

The meteorological towers measured temperature and relative humidity with Campbell Scientific DC215-L temperature/RH probes installed on a logarithmic vertical grid from 3 cm above the water to a max height of 258 cm (see Figure 10).

Figure 10. Transmit site M_1 (foreground) and M_{NPS} (background). Towers were identified as follows: M_1 (NRL tower #1, Tx site), M_2 (NRL tower #2, Rx site), and M_{NPS} (NPS tower, Tx site).

The probes were aspirated with a low-flow fan to maintain a flow of ≈2 m s-1 past the sensor. Analog wind speed and direction were measured with a Campbell 05106-L (RM Young) marine wind monitor. Water radiative skin temperature was measured with a Heimann KT18.85-II passive infrared sensor. Solar radiation was measured by a Kipp & Zonen CNR-1 pyranometer. Lastly, the Campbell sonic anemometer (CSAT3) and LI-COR (CS7500) were extended 2.5 meters over the water from an aluminum pole that was secured to the stationary dock next to the transmit site. Additional equipment used is listed in Table 1.

Table 1. Equipment listing, where *Locations* depicts possible areas in which units were deployed. Towers were identified as follows: M_1 (NRL tower #1, Tx site), M_2 (NRL tower #2, Rx site), and M_{NPS} (NPS tower, Tx site).

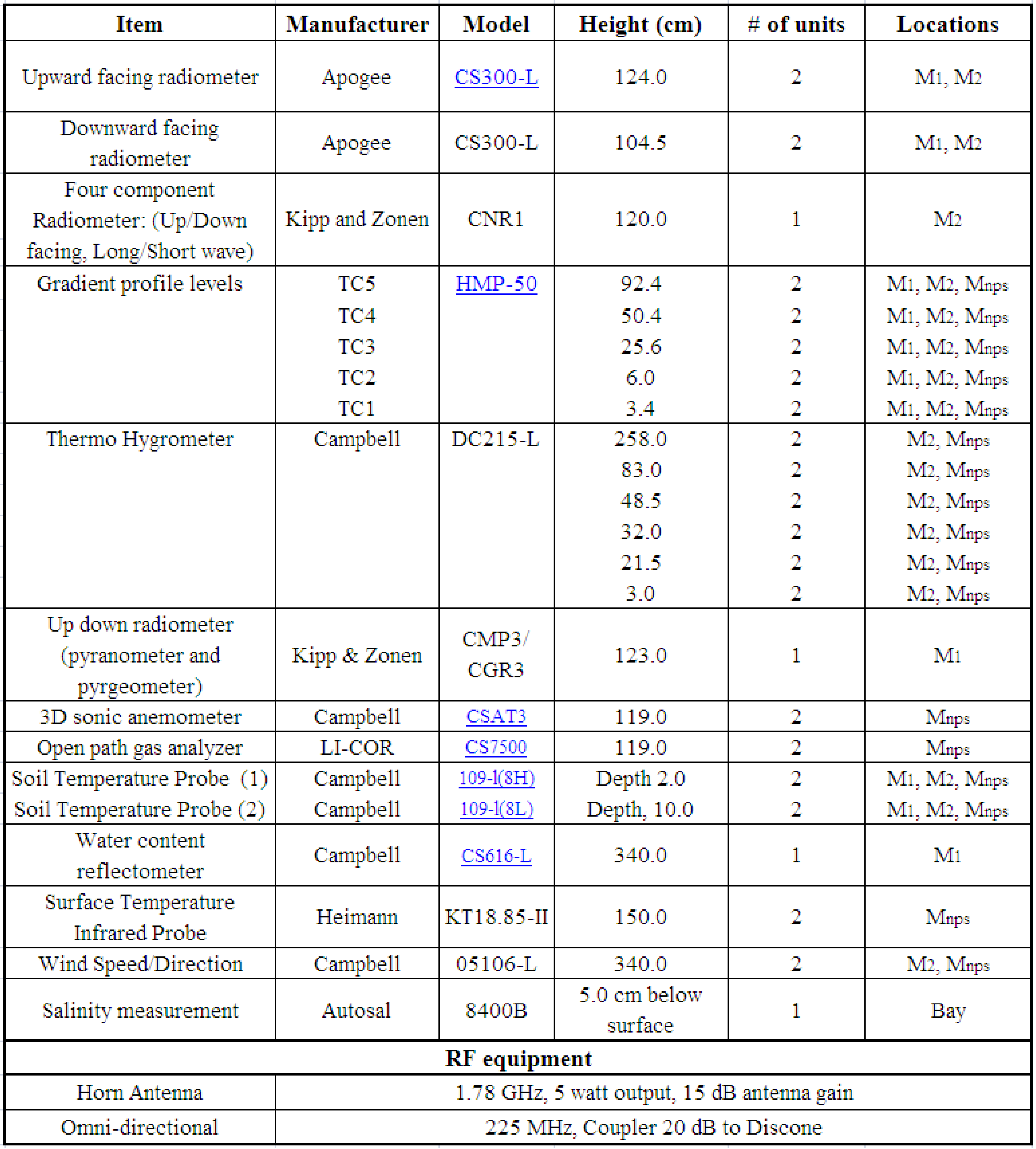

Item	Manufacturer	Model	Height (cm)	# of units	Locations
Upward facing radiometer	Apogee	CS300-L	124.0	2	M_1, M_2
Downward facing radiometer	Apogee	CS300-L	104.5	2	M_1, M_2
Four component Radiometer: (Up/Down facing, Long/Short wave)	Kipp and Zonen	CNR1	120.0	1	M_2
Gradient profile levels	TC5	HMP-50	92.4	2	M_1, M_2, M_{nps}
	TC4		50.4	2	M_1, M_2, M_{nps}
	TC3		25.6	2	M_1, M_2, M_{nps}
	TC2		6.0	2	M_1, M_2, M_{nps}
	TC1		3.4	2	M_1, M_2, M_{nps}
Thermo Hygrometer	Campbell	DC215-L	258.0	2	M_2, M_{nps}
			83.0	2	M_2, M_{nps}
			48.5	2	M_2, M_{nps}
			32.0	2	M_2, M_{nps}
			21.5	2	M_2, M_{nps}
			3.0	2	M_2, M_{nps}
Up down radiometer (pyranometer and pyrgeometer)	Kipp & Zonen	CMP3/ CGR3	123.0	1	M_1
3D sonic anemometer	Campbell	CSAT3	119.0	2	M_{nps}
Open path gas analyzer	LI-COR	CS7500	119.0	2	M_{nps}
Soil Temperature Probe (1)	Campbell	109-l(8H)	Depth 2.0	2	M_1, M_2, M_{nps}
Soil Temperature Probe (2)	Campbell	109-l(8L)	Depth, 10.0	2	M_1, M_2, M_{nps}
Water content reflectometer	Campbell	CS616-L	340.0	1	M_1
Surface Temperature Infrared Probe	Heimann	KT18.85-II	150.0	2	M_{nps}
Wind Speed/Direction	Campbell	05106-L	340.0	2	M_2, M_{nps}
Salinity measurement	Autosal	8400B	5.0 cm below surface	1	Bay
RF equipment					
Horn Antenna	1.78 GHz, 5 watt output, 15 dB antenna gain				
Omni-directional	225 MHz, Coupler 20 dB to Discone				

III. DATA PROCESSING

A. SUMMARY

The data that were collected during the Panama City Near-Earth Propagation Test (NEP-6) consisted of very high resolution (200 Hz) radio-frequency (RF) signals, turbulence and flux measurements, as well as reduced resolution (1 Hz) meteorological data. Sea surface level was measured every 6 minutes. Additionally, water samples for salinity measurements were obtained manually on a sporadic basis, but typically once each during the morning and evening time-frame. Due to the wide range of data resolutions, it became necessary to first establish a baseline resolution in the time series (in this case, 1 Hz), and then interpolate the coarse data sets to higher frequencies before filtering, or similarly, average the higher resolution data sets to match the desired 1 second time scale.

B. RF DATA PROCESSING

The RF data set consisted of transmit and receive power levels in dBm for both the 225 MHz and 1.78 GHz frequencies. This study focused on the 1.78 GHz portion as this is within the frequency band typical of most peer-to-peer wireless networks, particularly those with defense applications (Merrill et al., 2004, p. 36). Because both transmit and receive data were collected at a rate of 200 Hz and the length of the time intervals at which data were amassed ranged from a minimum of 12 hours to a 28-hour maximum, the data sets were necessarily large (on the order of 1 terabyte). Due to the difficulty of processing large files, these data were recorded in roughly one hour increments and stored in binary format to flash media. Each day, the LoggerNet protocol downloaded to a master computer where it was subsequently converted to an application-specific (.dat) data file.

The first step in processing these data was to convert them from the proprietary .dat format to MatLab™ compatible .mat format. This was accomplished using a script file developed by Mr. Vincent Wong of Naval Research Laboratories, Washington, DC. Once converted, each hour was plotted over time to provide a rough estimate of transmit, receive, and net loss levels. Both transmit and receive data were recorded as dBm, which is the power ratio in decibels (dB) of the measured power referenced to one milliwatt (mW). This proved to be the most convenient unit of measure of absolute power because of its capability to express both very large and very small values in a relatively short form. Net propagation loss was the parameter selected to indicate the attenuation of an RF wave propagated in the given environment. Net propagation loss is the difference between transmitted power and received power. These calculations yielded the net loss vector in dB, a dimensionless unit that quantified the ratio between these two values. At this point, obvious outliers that were greater than 2 standard deviations from the mean were removed using basic MatLab™ indexing commands. Next, the hourly data files underwent initial smoothing to accommodate the expected shot and thermal noise from the transmitting RF diode. This noise is clearly depicted in Figure 11 as a 0.5 dBm fluctuation (in blue) following the received power trend.

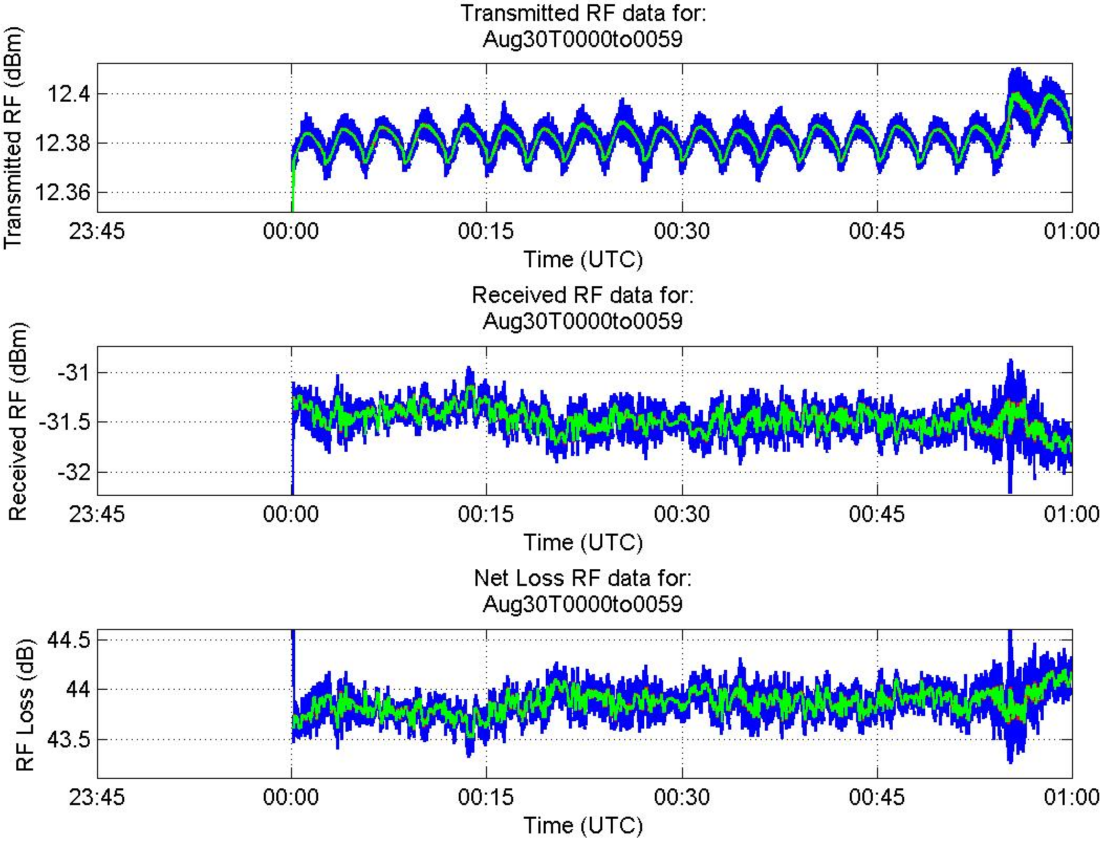

Figure 11. Representative sample of raw (blue) and smoothed (green) RF data.

Upon completion of this initial smoothing, the loss vector from each hourly data set was filtered (using various window sizes), and then sampled to achieve an intermediate resolution of 10 Hz. Window size was selected manually in order to minimize side lobe influence on the running mean and consisted of starting with a very wide filter and then gradually reducing the width until the desired resolution was obtained. This yielded a vector approximately 24 million data points in length and was necessary due to computational constraints. Data treatment continued by first calculating the best fit polynomial trend line (in this case, an 8th order), subtracting out this trend and then filtering the output over various, relatively large window sizes. Higher-order polynomial trend lines did provide slightly lower χ^2 error values, but as Figure 12 depicts, the relative reduction in error for each subsequent increase in order was insignificant beyond the 8th order. This de-trending technique ensured maximum filtration of noise from the actual data, while maintaining the dominant diurnal oscillation, as well as to prevent those time periods in which data were missing from overly influencing the filtered output.

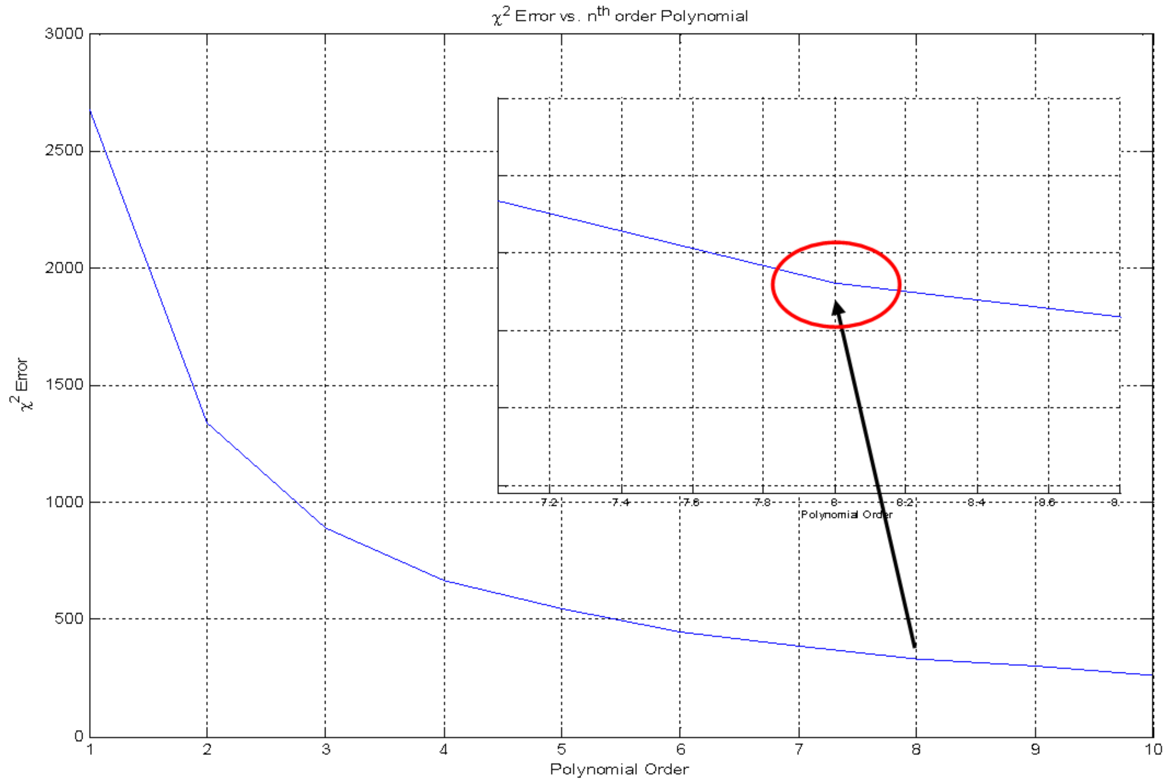

Figure 12. Plot of χ^2 difference between raw data and 8th order polynomial, justifying selection of polynomial order.

The polynomial trend line was added back in and the data were interpolated onto a 1 Hz resolution time series, using **`interp1`** (a built-in function utilizing linear interpolation). All filtering calculations used the MatLab™ function **`filter`**, which utilizes rectangular amplitude weighting to generate a simple running mean of the surrounding data points, as follows: $y_n = \Sigma c_k \, x_{n-k} + \Sigma d_j y_{n-j}$, where d=zero, c=1/(window order), and k goes from 1 to window width. Window order was linear, and widths were selected manually based on completeness of data and resolution.

C. METEOROLOGICAL DATA PROCESSING

Meteorological data were collected at 200 Hz, 1 Hz and greater time scales—each frequency class was treated differently. The purpose was to present the greatest amount of information that could reasonably be assimilated and compared to the RF data series. The 200 Hz turbulence and flux data were processed and analyzed in a similar manner to the RF data series, however some effort was made in reducing the amount of information lost to filtering and sampling as this data set was not nearly as robust as the one previously discussed due to the "averaged" nature of these measurements. Data loss was reduced by limiting the number of iterations of filter/sampling as well as fitting of polynomial curves. This allowed the use of a "noise reduced" (or low pass filtered) data set that still contained the important variations, while removing the higher frequency components that were not of interest. The 1 Hz data were derived from measurements on two full towers and one partial meteorological tower as detailed in Table 2 (next page).

Table 2. Tower sensor profiles listing, towers were identified as follows: Tower1 (NRL tower #1, Tx site), Tower2 (NRL tower #2, Rx site), and TowerNPS (NPS tower, Tx site).

	Tower ID		
	Tower1	Tower2	TowerNPS
Temp/RH Profile (cm)	4.0 15.0 27.0 53.0 93.0	3.0 21.5 32.0 48.5 83.0 258.0	11.5 18.5 34.0 66.0 130.5 247.0
Water Temp Profile (cm)	4.0 8.0	4.0 8.0	4.0 8.0 18.0
Wind Profile (cm)	165.0 153.0 102.0		340.0

On the transmit side of the experiment layout, the floating dock supported the RF transmitters, two temperature and relative humidity (RH) probe suites situated over a nominally logarithmic scale (from 3.0 cm to 258.0 cm), as well as various meteorological equipment sensing wind and rainfall. Temperature and RH was smoothed using **`filter`** with a rectangular window size of 1000 data points, and then sub-plotted against RF loss for comparison and analysis. For derived meteorological variables such as specific humidity (q), modified index of refraction (M), and gradients, measured data were initially used and then the output was filtered and interpolated in a manner similar to temperature and RH.

Wind data were integral to the analysis and were processed as follows. Raw wind speed and directional data were first converted to component vector form (**u,v**) using the MatLab™ script **`uv.m.`** Noise and aberrant data were removed from the data set by way of two mathematical methods: the first was filtration of a simple scalar mean and the second utilized the individual **u** and **v** components to calculate a vector mean. Wind direction was averaged using a unit vector technique to avoid the problem of averaging around North, e.g., preventing 359˚ and 001˚ from averaging to an obviously incorrect 180˚. Using the component vectors safeguarded against this and ensured a truthful representation of the dominant winds experienced at the transmit site over the course of the three day trial. Both resulted in similar time-series plots (Figure 13); however, the calculated amplitude in the vector mean method was reduced by a factor of 0.2.

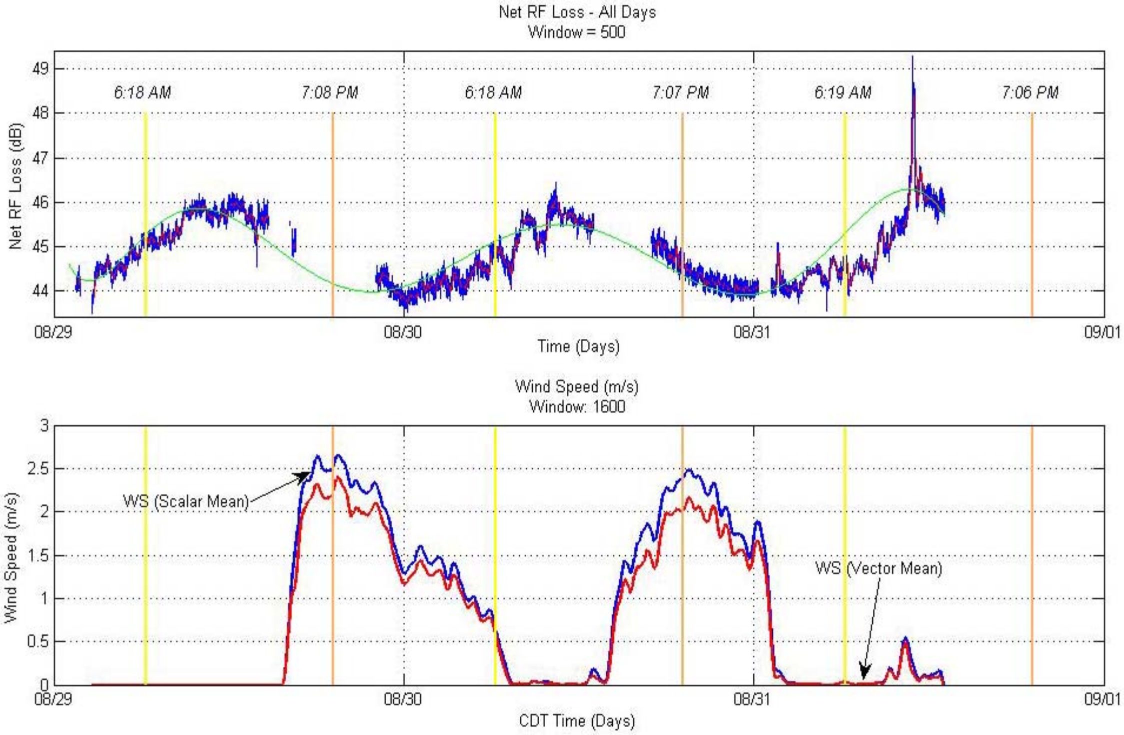

Net RF Loss - All Days
Window = 500

Wind Speed (m/s)
Window: 1600

Figure 13. Sub-plot comparison of RF loss to smoothed wind speed.

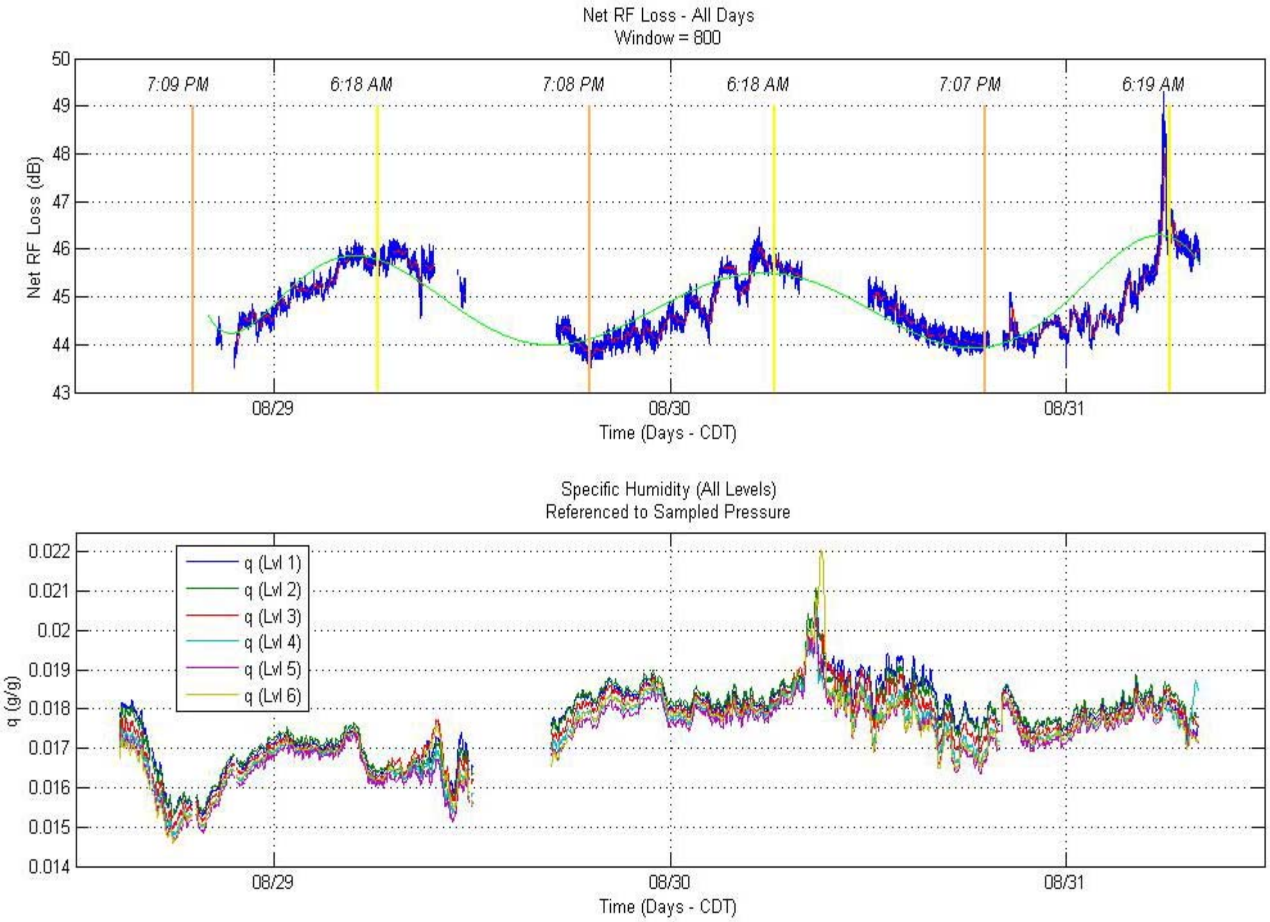

Figure 14. Sub-plot comparison of RF loss to q.

Specific humidity (q) and saturation vapor pressure (e) were first calculated using raw values for temperature, relative humidity, and pressure, with subsequent output being filtered and then sub-plotted against RF loss. Window size was selected based on maximum smoothing of the time series, while still minimizing data loss. Additionally, to aid in data assimilation and pattern recognition, q, T, M, and RH were also plotted against an arbitrary reference level (see Figure 15). This was simply the centermost measurement level for any given data set.

Modified index of refraction was calculated using the **`mod_refract.m`** function by Bean (1966), which is actually identical to Equation (13) with the exception of the last decimal of accuracy. A separate script for this equation was not written simply because the built in function was sufficient for our observations. Also, due to the close ranges and low heights, Earth's curvature was not important for this experiment; a base height of 0 meters was assumed for *z*, thus in all actuality this calculation provided *N*, refractivity—a difference which did not affect data analysis.

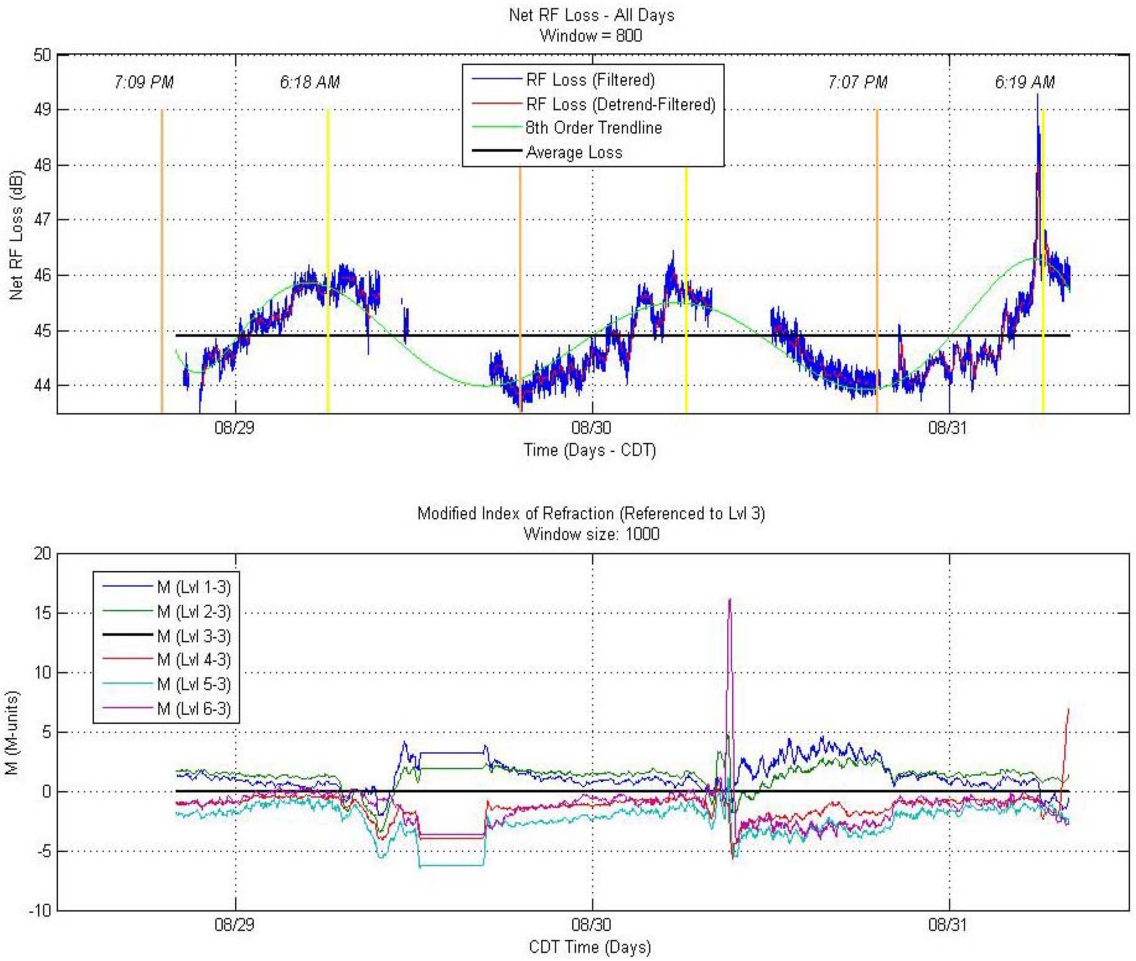

Figure 15. Sub-plot comparison of RF loss to referenced M.

Finally, internal water temperature and surface skin water temperature values were gathered via submerged thermistor probes and two passive IR sensors. Processing of this data was the same as in the case of air temperature and relative humidity.

D. OCEANOGRAPHIC DATA PROCESSING

Tidal data had the largest apparent effect on interference and attenuation in the transmitted RF wave. This information was obtained from two sources: the first and primary data set was of actual tides measured on site by means of a SR50A Sonic Ranging Sensor that was situated on the NRL tower. According to the Campbell Scientific data sheet (2009), this sensor emits a 250 mA ultrasonic pulse that enables height measurements with an accuracy of ± 1 cm.

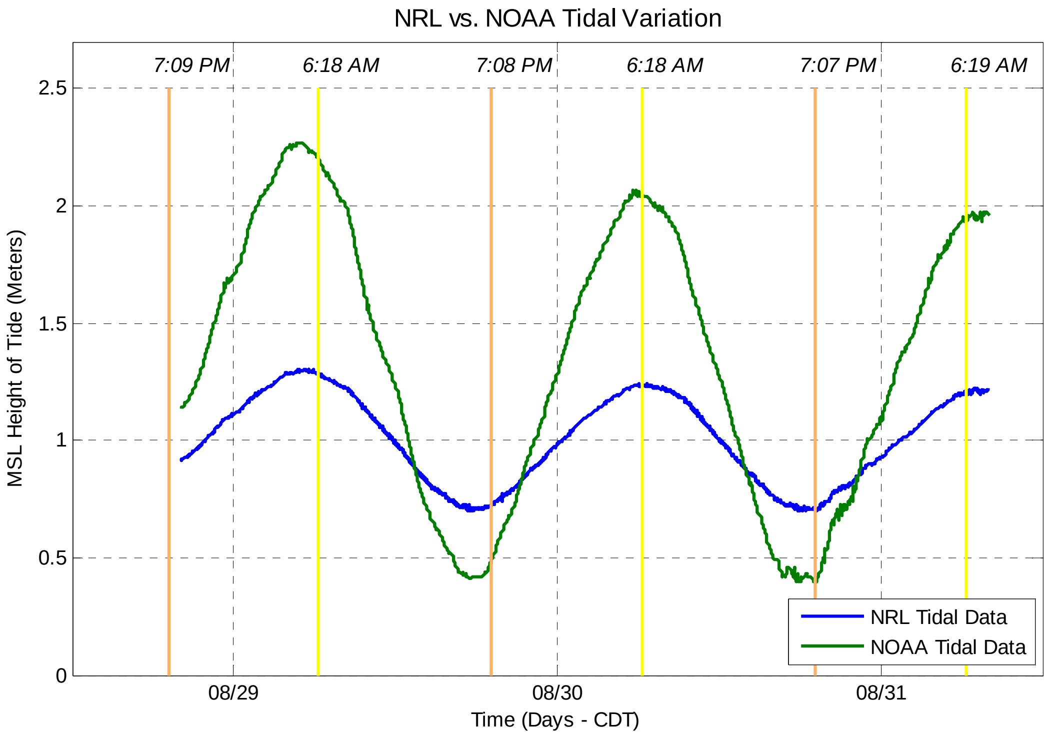

Figure 16. Time-series comparison of NOAA and NRL tidal data.

A secondary data set was drawn from a NOAA tidal observation station based in Panama City, FL (Station ID: 8729108), which was located approximately 5 n mi. Southeast of the NEP-6 experiment site. As one would expect, the range of diurnal oscillation of the more sheltered NRL tidal data was much reduced when compared to the NOAA tides (which were collected at the inlet to St. Andrews Bay), and also possessed a lower (by 0.299 meters) mean magnitude (Figure 16). Due to their low resolution, both data sets were interpolated onto a one second time grid in order to match the RF data series, although filtering was unnecessary given their relative clarity and lack of noise.

Salinity samples were collected at both the transmitter and receiver sites, and generally in the morning. Each sample was tested on an "AutoSal" 8400B Laboratory Salinometer which has a measurement accuracy of < ± 0.002 Equivalent PSU according to the Guildline Instruments data sheet (2002), and is obtained via calculation and substitution in the Bennet equation. It was difficult to garner any sort of understanding from this data set due to its sporadic nature and low number of data points recorded (blue circles above).

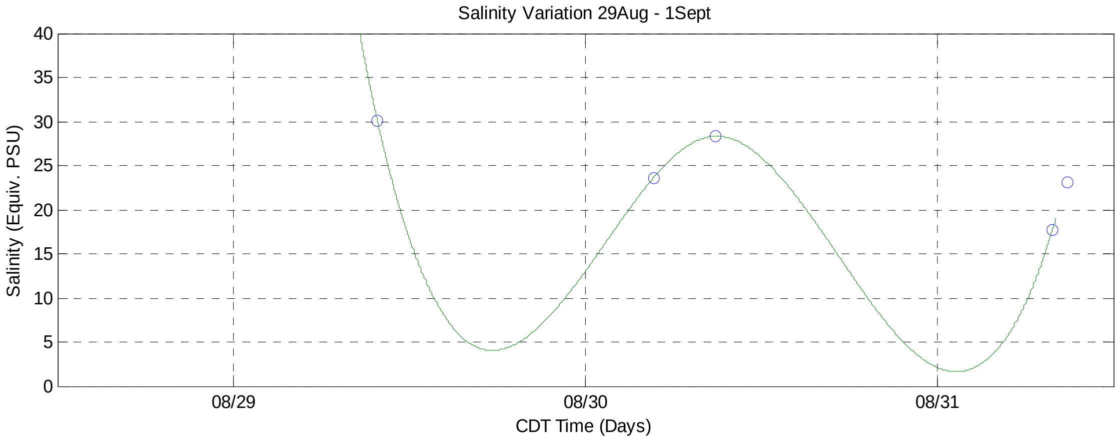

Figure 17. Time-series plot of salinity values (blue) and trend line (green).

However, some effort was made (using the **`spline`** command) in fitting a recognizable curve (green line) to this sparse data set in order to enable broad comparison to both RF and meteorological data (see Figure 17). Akin to the aforementioned data processing techniques discussed, salinity values were interpolated onto a 1 Hz grid and then sub-plotted against the other measured variables. This result proved to be less than perfect since **`spline`** only calculates a cubic spline interpolation of the data and is limited by the size of the data vector. Nonetheless, it did provide the basic insight that salinity fluctuated approximately in time to tidal influence (as expected), and though we suspect it may have been related to the observed lag between RF loss and tides, it is unlikely that salinity played a direct role in RF propagation loss as shown by the single variable correlation calculations.

IV. DATA ANALYSIS

A. SUMMARY OF METHODOLOGY

The primary goal of the analysis was to identify the variables that were most correlated with RF loss variations. The variance of the RF data that can be explained (i.e., correlated to) by a particular environmental variable can be *subtracted out*, leaving residuals that can then be further correlated with other variables. Whatever variance that remains after testing with all variables is ideally a small amount and represents unknown effects. This study utilized a multi-tiered process of statistical and data processing techniques as follows: a basic rough data preview, a smoothed data sub-plot comparison via visual inspection, linear (through scatter plot trends) and sine wave correlation, and finally, physical geometry association and subsequent modeling of the data.

B. RAW DATA PREVIEW

One of the more difficult challenges in working with so much measured information was in determining what fraction of the data were vital, and which were extraneous and therefore unneeded. While in the end the size and scope of the data sets were reduced by way of the previously discussed methods, it was still considered essential to provide an overview of the information as presented in its raw form. The difficulty in this was that data were collected at 200, 1, and 1/360th Hz, and that each individual data set was not necessarily complete, hence, the need for interpolation of the longer (200 Hz) and shorter (1/360th Hz) data sets to a common time-series. The reference level of 1 Hz was selected as because all of the meteorological data were collected at this rate, it provided sufficient resolution for the variables considered, and did not require excessive CPU processing time.

Computational constraints were accommodated by merely loading small slices of the data (typically hourly but, for some lower resolution files, longer times were used) at a time (Figure 18, next page). Two-hundred Hz data—particularly the RF signal files—were loaded, plotted, and saved in hourly segments via an automated loop.

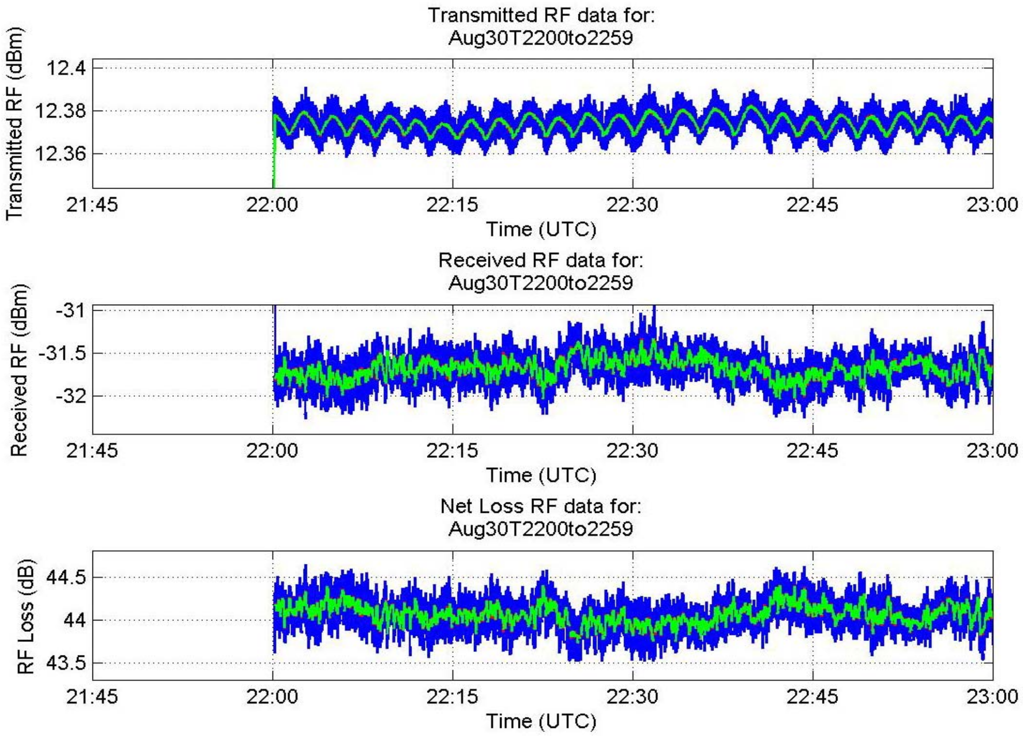

Figure 18. Hourly segment sample of RF loss.

Visual inspection of these graphics provided the following insights:

a) High frequency variation on the order of 0.1 to 0.5 dBm, was noted on all RF plots. This is comprised of both shot noise and thermal noise emitted by the RF diode. These levels are consistent with expected shot noise (typically very small) and the contribution from thermal noise. The magnitude of thermal noise will increase as environmental temperatures rise, hence the pseudo-correlation to time of day.

b) The two- to three-minute oscillations apparent in the transmit plot were likely due to slight power draw fluctuations caused by the air conditioner that was used to cool the transmitter. Internal environmental control was imperative in order to protect the transmitter, preserve the positive signal to noise ratio, and finally to protect the wireless radios that were transmitting data between the two sites. Additionally, some fluctuation in the power supply was expected due to the limited number of available receptacles.

c) Known power outages and time periods in which the transmitter was switched off for safety reasons (as shown in Table 3) were correlated to empty intervals in the data (Figure 19).

Table 3. Table of known transmitter interruptions.

Time Range (CDT)	Reason for Outtage
28Aug09, 1900-2359	Power fluctuations due to fine tuning of Tx A/c.
29Aug09, 0000-1300	Power fluctuations due to fine tuning of Tx A/c, and switch from grid to generator power.
29Aug09, 1300-1325	Realignment of Young wind monitor.
30Aug09, 0700-0900	Power grid failure, switch from generator back to grid power.
30Aug09, 0900-1000	Swimmers in water.
01Sep09, 0600-0700	Swimmers in water.

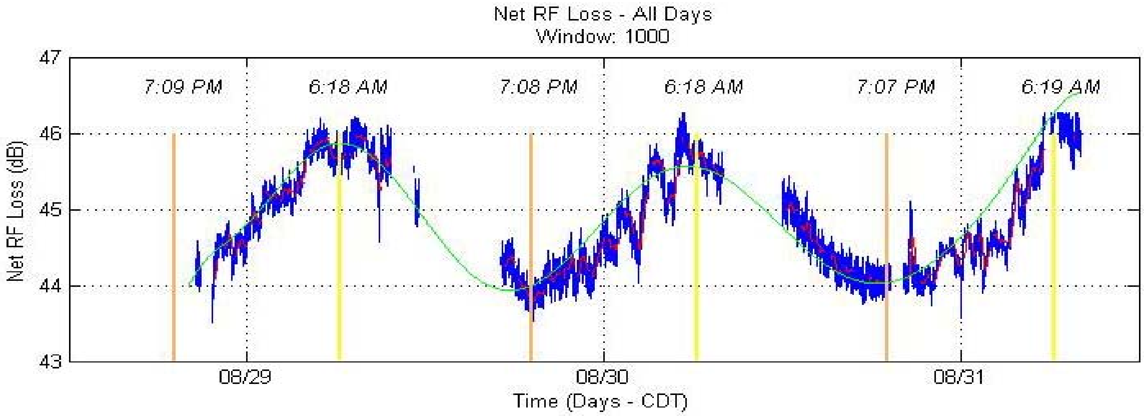

Figure 19. Three-day time-series of RF net loss depicting times of missing data.

While visual inspection of hourly data did permit depiction of fine scale variability, it proved unwieldy for observing the dominant trends in the data. A three-day plot of the RF net loss time series was finally realized thru exploitation of the sampled version, which had been filtered in such a manner as to reduce the associated RF noise, yet still allow the variance of the "unknown" drivers to have an effect. Moreover, by superimposing the sunrise and sunset times onto the three-day plot, it became obvious that the periods of greatest and least loss in received power occurred on a nearly perfect 24-hour cycle, and corresponded to sunrise and sunset. It was also noted that while the RF loss vector seemed to follow this dominant 24-hour sinusoidal trend, there were also smaller scale variations that could not be explained exclusively by the above three observations. This predominant variability would ultimately be explained via the analysis as follows.

C. SUB-PLOT COMPARISON OF VARIABLES

Proper smoothing and filtering of the meteorological and oceanographic variables before they were compared to the RF loss vector were of utmost importance to this portion of the analysis. Akin to the raw data analysis section, computational expense (i.e., time) had to be considered, and thus either hourly segments or a course resolution of three-day samples were used. Initially, each meteorological variable was simply sub-plotted against the net loss vector on the same time series grid. This yielded an excess of figures to review, but very few variables that clearly stood out as having a definitive affect. Tidal fluctuation, solar radiation, and sampled air pressure seemed to have the greatest visual correlation, while temperature and relative humidity provided relatively high *r*-values.

The *r*-values for each of the above data sets were calculated using the MatLab™ command **`corrcoef`**, which is based on the Pearson product-moment correlation coefficient (PMCC). By definition, this is the covariance of the two variables divided by the product of their standard deviations:

$$\rho_{X,Y} = \frac{\operatorname{cov}(X,Y)}{\sigma_X \sigma_Y} = \frac{E[(X-\mu_X)(Y-\mu_Y)]}{\sigma_X \sigma_Y}, \tag{10}$$

where $\rho_{X,Y}$ is the population correlation coefficient. By substituting the estimated covariances and variances based on the sample, the above gives the *sample* correlation coefficient, commonly denoted *r*:

$$r = \frac{\sum_{i=1}^{n}(X_i - \bar{X})(Y_i - \bar{Y})}{\sqrt{\sum_{i=1}^{n}(X_i - \bar{X})^2}\sqrt{\sum_{i=1}^{n}(Y_i - \bar{Y})^2}}. \tag{11}$$

where X_i, Y_i are paired sample data, $\bar{X}, \bar{Y}$ are the sample means, and *n* is the number of data points in the sample (Cohen, 1988).

In summary, the PMCC *r*-values provided guidance as to the best direction to follow when sifting through the numerous meteorological and oceanographic variables. The data that showed the most promise were scatter plotted against both the smoothed RF loss data, as well as the calculated residuals of the loss data. The intent was to find a linear relationship between the dependent and independent variables. Efforts were initially thwarted due to outliers that were missed during the smoothing process, as illustrated in Figure 20 (next page) however these extraneous data points were removed in subsequent iterations and correlation processing was much improved.

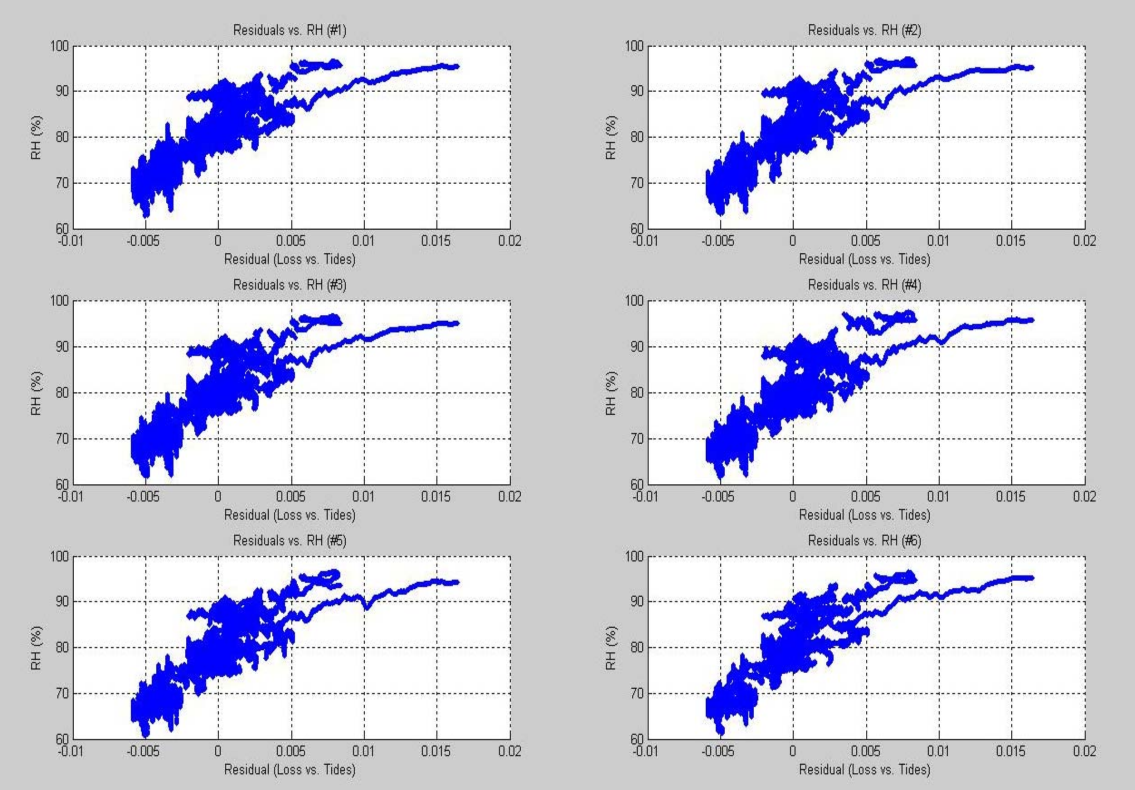

Figure 20. Scatter plot of RH (raw with outliers) at each level to the functionally dependent residuals of RF loss vs. tides.

The greatest advancement at this juncture was in removal of data outliers, confirmation of certain variables that would not have an impact on RF loss, and finally, by the positive and linear relationship between propagation net loss and tidal height.

D. VARIANCE REDUCTION TECHNIQUES

Upon completion of scatter plotting of the residuals to dependent variables, we found that antennae height change as a result of tidal flow had the largest correlation with (i.e., explained the most) variance detected in the RF loss data vector. In order to quantify the level of influence this and other variables had, two techniques were employed:

1) single variable correlation via scatter plots, and

2) best fit sine waves.

Unsurprisingly, both yielded similar results, however for reasons of efficiency, the former method was more prevalently employed.

1. Linear Trend-Line Correlation

To correlate via scatter plots first the variance (σ_0^2) of the data set was calculated using the MatLab™ command **`var`**, which served as a test bench mark for subsequent iterations. This command uses the standard definition for variance,

$$\mathrm{Var}(X) = \mathrm{E}[(X-\mu)^2] \tag{12}$$

where E[•] is the expected value or mean, X is the random variable and μ is the sample mean. Hence, the variance is a measure of the amount of variation within the values of that variable (Cohen, 1988). Next, smooth RF data were plotted against one of the dependent variables and a linear trend line was extracted (Figure 21). This basic formula (**y**=m**x**+b) was then evaluated at each data point and subtracted from the original loss vector. The resulting vector of new loss values was dubbed *epsilon 1* (ε_1) and possessed an updated variance as calculated using the above command, **`var`**.

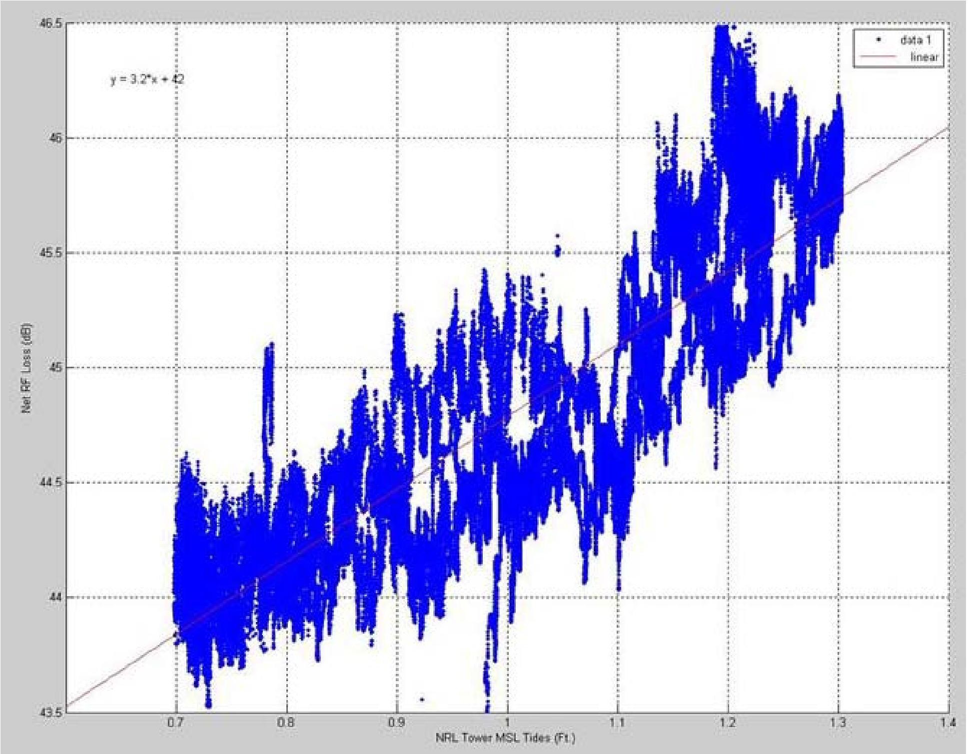

Figure 21. Scatter plot of RF loss to NRL derived MSL tides with linear trend line.

If by way of application of Equation (13) the variance was reduced, then that variable was considered to have had an effect and the problem became simply one of finding the variable of greatest consequence.

$$\begin{gathered}\text{Loss} - (a_1+b_1{*}\text{Var}_1) = \varepsilon_1\text{, where } \varepsilon_1{:}\sigma^2{}_1 \\ \text{Loss} - (a_1+b_1{*}\text{Var}_1) - (a_2+b_2{*}\text{Var}_2) = \varepsilon_2\text{, where } \varepsilon_2{:}\sigma^2{}_2 \\ \vdots \qquad\qquad\qquad\qquad \vdots\end{gathered} \tag{13}$$

In this manner, the preliminary variance of 0.4676 dB was immediately reduced (by 74.5%) by removing the effect of antennae height fluctuation (Figure 22). It should be noted that the tidal data used was taken from the onsite NRL tidal sensor and not from the NOAA observation station.

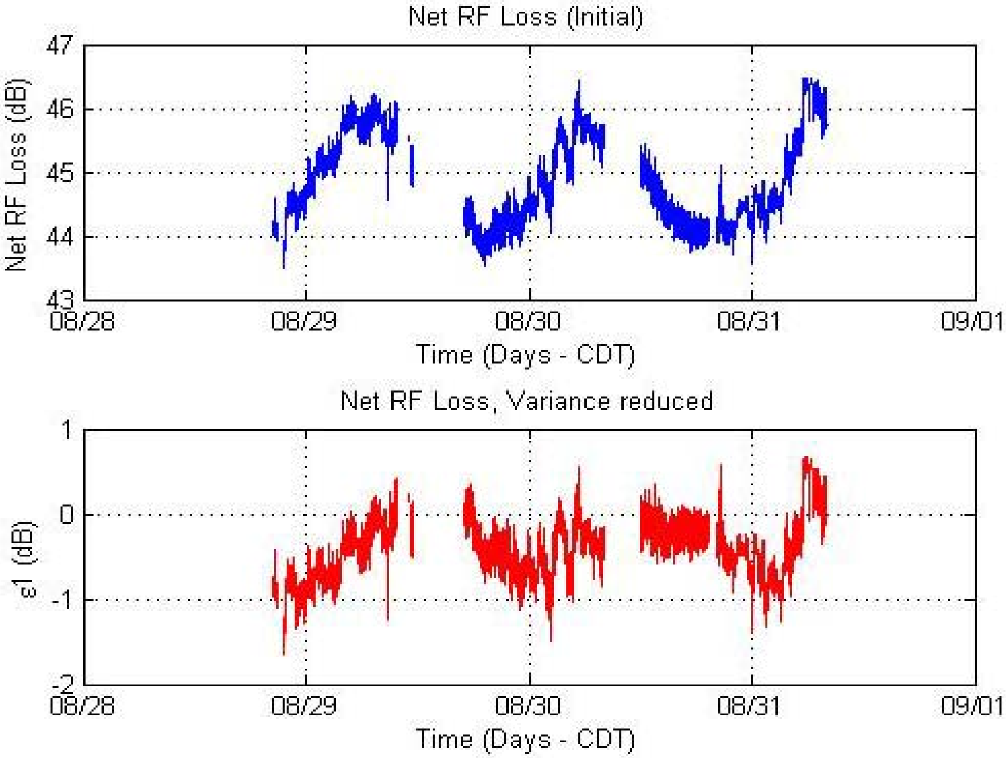

Figure 22. Sub-plot comparison of net loss and ε_1.

Figures 23 through 25 depict pictorially the processing procedure. Note the still oscillatory nature of the ε_1 vector and rapid decrease in "noise" amplitude. The first was a characteristic that persevered through several cycles of this process while amplitude degenerated more slowly with each subsequent application. The raw variance of ε_1 was 0.1090 dB.

Solar radiation displayed a strong correlation (PMCC *r*-value of ≈1.0) that was difficult to ascertain visually, yet still produced statistically significant variance reduction.

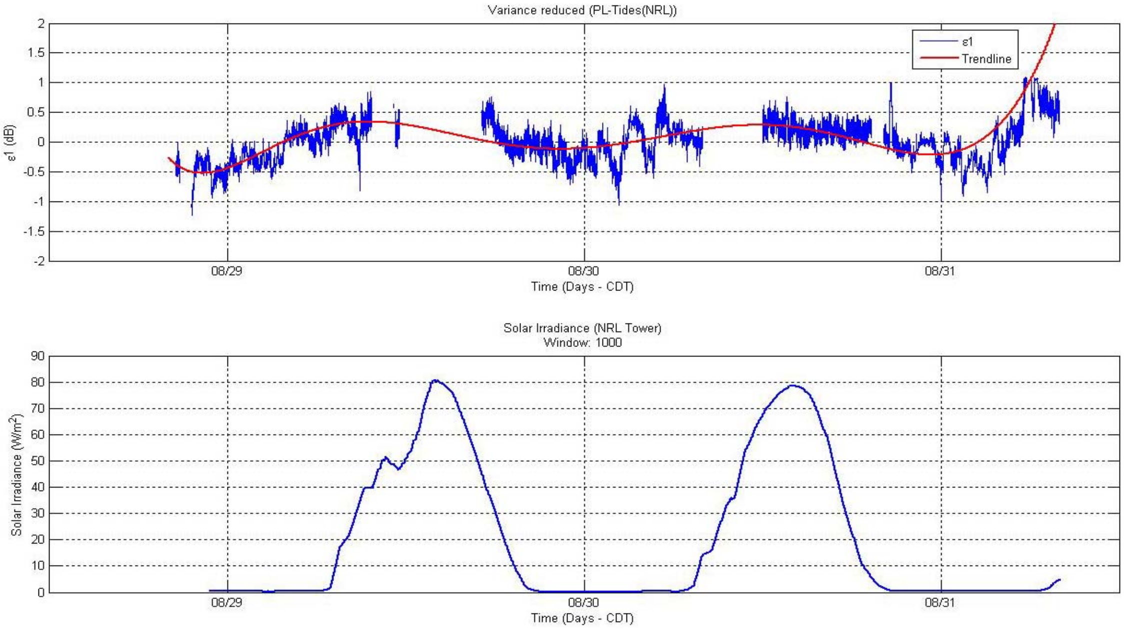

Figure 23. Time-series sub-plot of ε_1 to solar irradiance.

Scatter plotting ε_1 against solar irradiance illustrated this linkage:

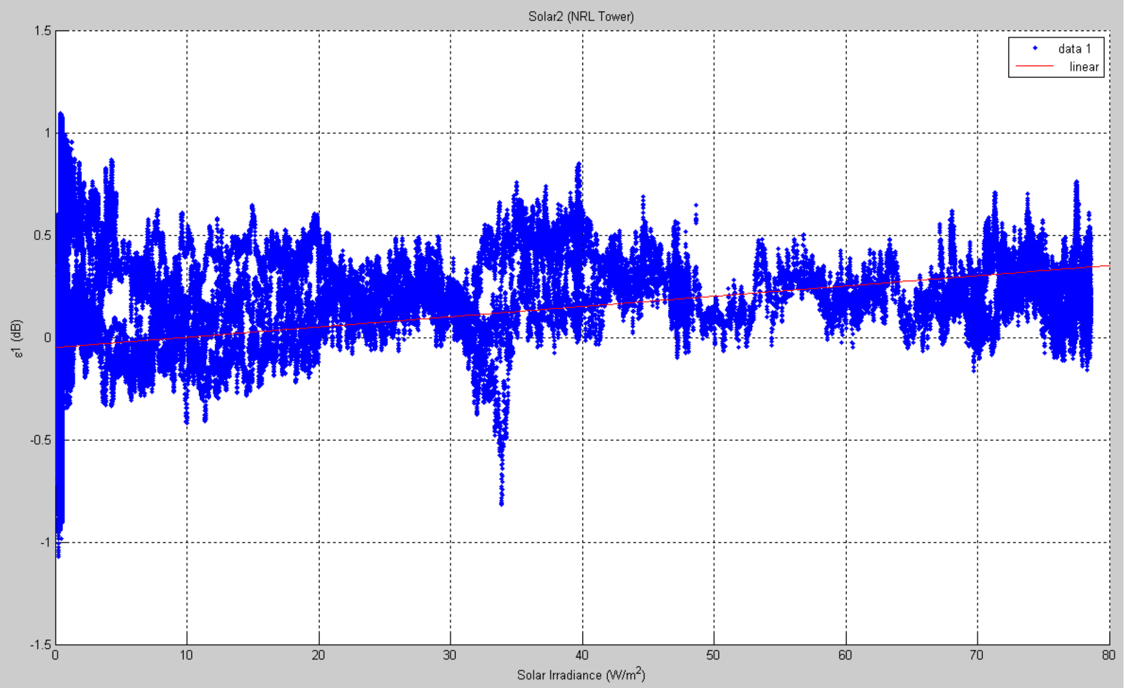

Figure 24. Scatter plot of ε_1 to solar irradiance.

Ultimately, ε_2 reduced overall variance to 0.0917 (dB) and compared very closely to ε_1.

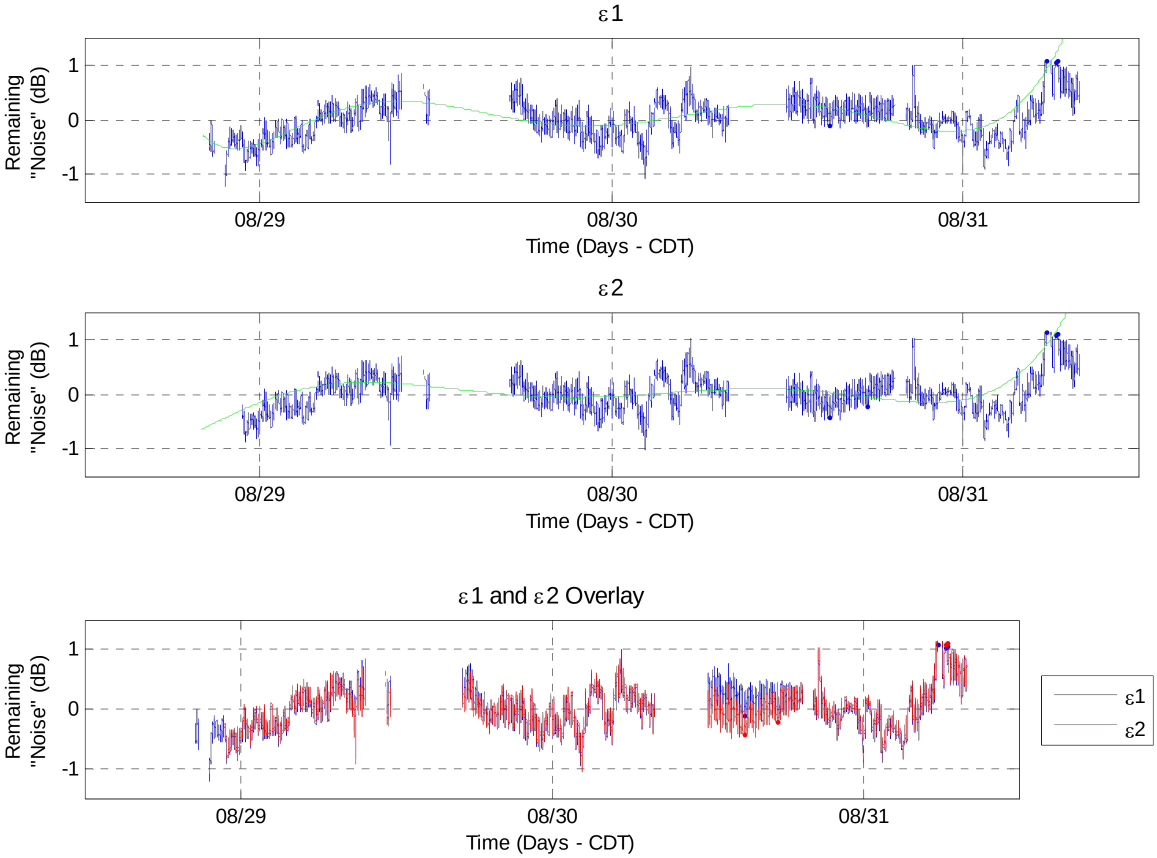

Figure 25. ε_1 to ε_2 sub-plot comparison and overlay plot.

Subsequent iterations were similar in nature and resulting single variable variance reduction is summarized in Table 4. Note that Air Temperature and RH produced exactly the same degree of variance reduction.

Table 4. Summary of variance reduction where ε is the resultant vector after removing the variance attributed to that variable, *Variance* is the raw value for each ε vector and *% Variance Reduction* is the overall percent reduction from the original variance.

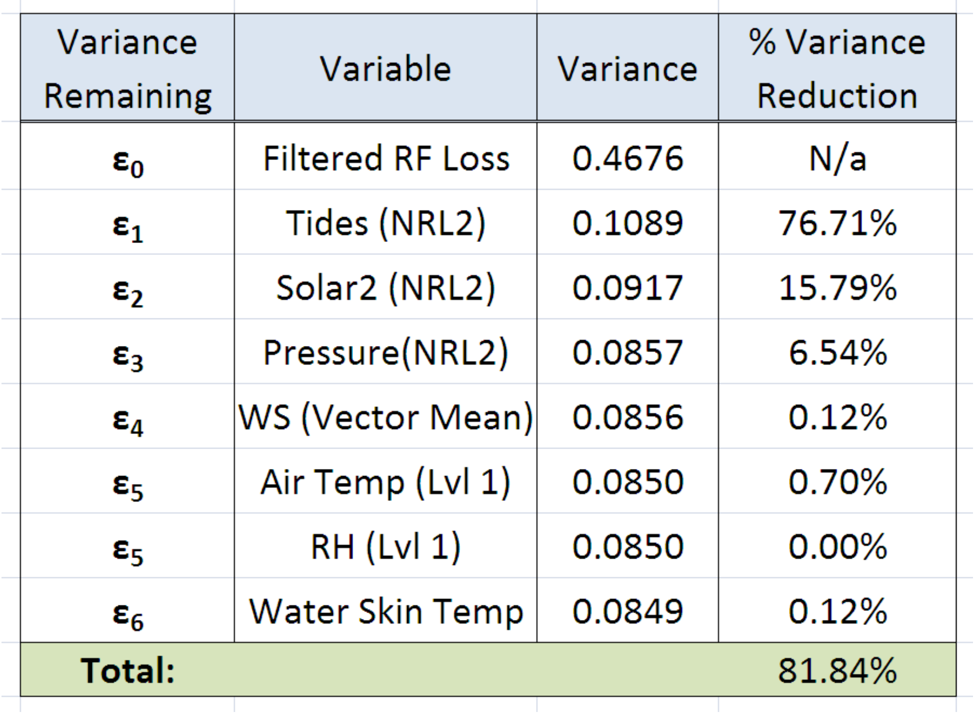

Variance Remaining	Variable	Variance	% Variance Reduction
ε_0	Filtered RF Loss	0.4676	N/a
ε_1	Tides (NRL2)	0.1089	76.71%
ε_2	Solar2 (NRL2)	0.0917	15.79%
ε_3	Pressure(NRL2)	0.0857	6.54%
ε_4	WS (Vector Mean)	0.0856	0.12%
ε_5	Air Temp (Lvl 1)	0.0850	0.70%
ε_5	RH (Lvl 1)	0.0850	0.00%
ε_6	Water Skin Temp	0.0849	0.12%
Total:			81.84%

This technique worked well primarily due to its ease of use and reasonably solid statistical significance based on the large sample size and outlier testing via scatter plots. However, this still does not fully answer the question of variability in the data set simply because it deals only in the single variable domain and the independence requirements may not have been met. This variance is illustrated in the first three variables used to reduce variance, in that they all follow a roughly diurnal cycle.

2. Best Fit Sine Wave Correlation

The alternate method of fitting a sinusoid to the data set was effective because of the cyclic nature of the majority of the measured variables. It also possessed the added benefit of extrapolating between holes in the data set by following the dominant trend (thus making it easier for the eye to see), and in being rather outlier resistance…although at times these benefits were outweighed by the relative difficultly and tediousness of the process.

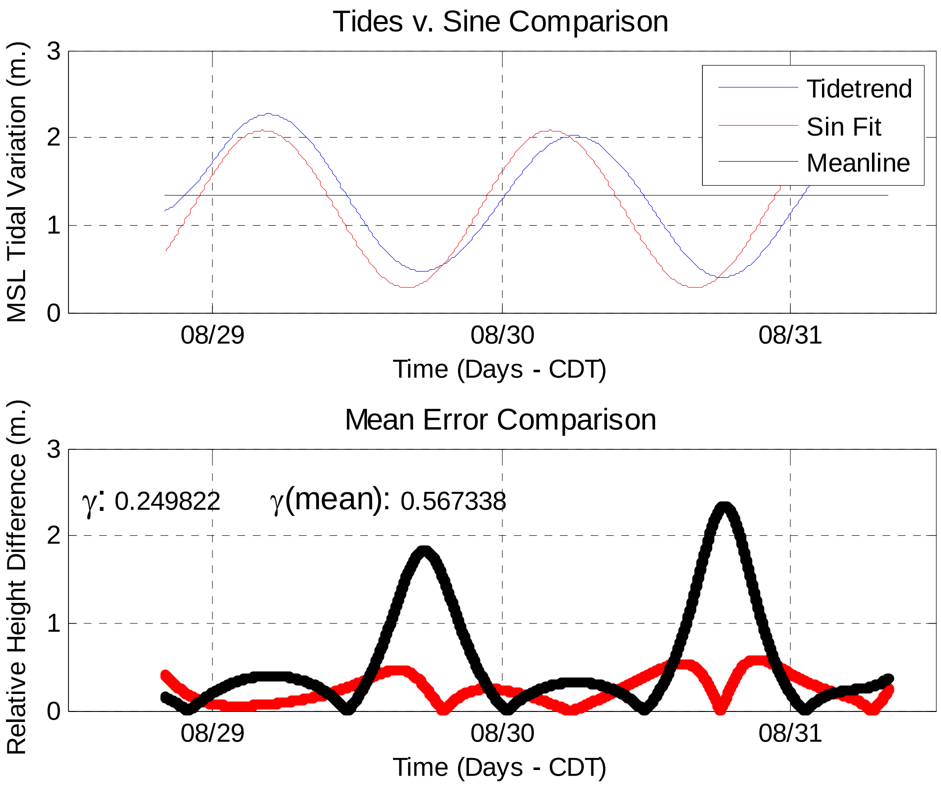

Figure 26. Best fit sin wave correlation via **datacorr6.m** with mean relative error between fit and trend line (red) and mean relative error between mean line and trend line.

First, a dependent variable (tides, air temperature, etc.) was plotted against the RF loss vector. If a similar trend was noted in the dependent variable, a sine wave was fitted to the data (as shown in Figure 26). To enable this fitting process, a MatLab™ script **`datacorr6.m`** was used to minimize the relative error between the modeled variable and the actual variable in the following manner. A generic sine wave (sine$_{\text{fit}}$) was constructed with variables for frequency, amplitude and phase shift:

$$\sin_{\text{fit}} = a + b * \sin(f * t + \phi), \tag{14}$$

where
a = centerline of sine wave
b = amplitude of the wave
t = time-series
f = frequency of operation
φ = phase shift

By manipulating these variables manually, the generic waveform was constructed to closely resemble the dependent variable. Relative error between the actual and modeled waveform was summarized in the "Mean Relative Error," γ in Equation (15):

$$\gamma = \left| \frac{(X_{dep} - X_{mod})}{X_{dep}} \right|, \tag{15}$$

where
γ = mean relative error
X_{dep} = dependent variable
X_{mod} = modeled waveform

Additionally, the relative error between the measured data and a mean line of said data $(\overline{X}_{dep})$ were used to provide reference as to the level of improvement the sine wave fit provided over a simple average:

$$\gamma_{mean} = \left| \frac{(X_{dep} - \overline{X}_{dep})}{X_{dep}} \right|. \tag{16}$$

This process yielded the coefficients necessary to evaluated the modeled function and subtract it from the original function, thereby reducing overall variance. Just as in the linear correlation method, this new epsilon vector possessed an updated variance that was ideally less than the original.

E. PHYSICAL GEOMETRIES ASSOCIATION

The correlation techniques described above provided some insight to the base cause of the RF loss wave fluctuation. Unfortunately, the magnitude of variance reduction by these techniques was ultimately limited and further application yielded results of dubious quality and validity.

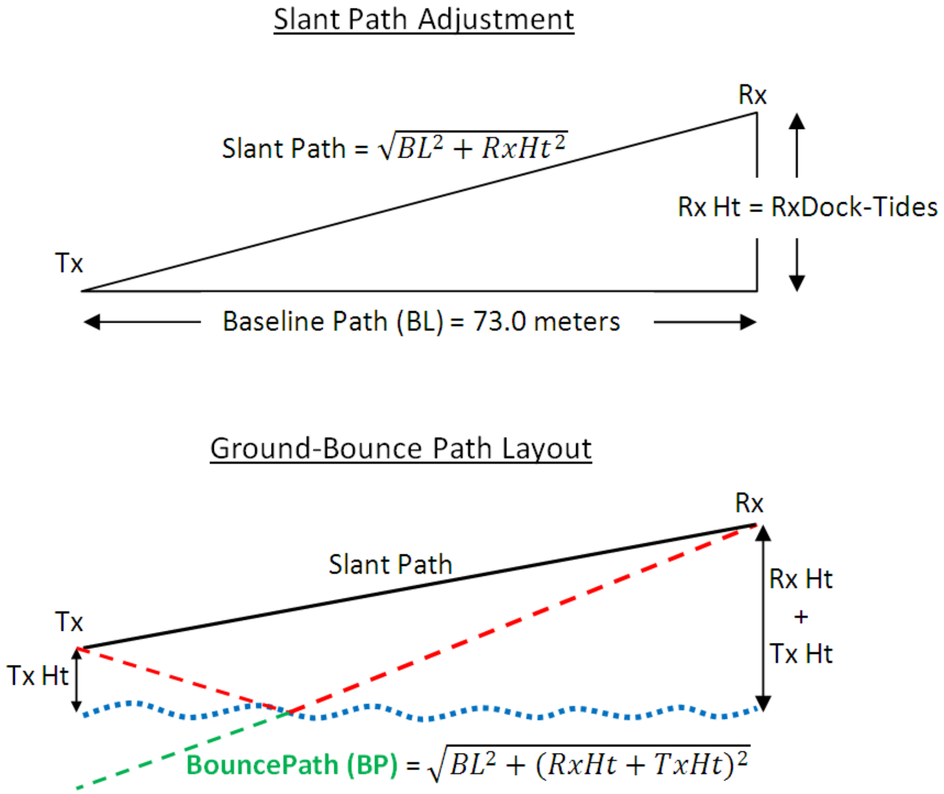

Figure 27. Trigonometric relationship between direct and surface scatter rays from transmitter to receiver. (Red is the actual ray, green is the virtual reflected ray.)

In order to explain the residual variance due to tidal influence (See Table 4), attention was turned to the physical relationship between direct path and single reflection scatter-path rays (Figure 27). The direct path length between the transmitter and receiving unit was measured via a laser range finder and found to be 73 meters. This rough slant path measurement was obtained from the receiving site, (approximately 2.667 meters above the water) to the transmitter, which was situated approximately 0.3028 meters above the water. Due to the change in tidal height above mean sea level (recall, the transmitter was mounted to a floating dock), this dimension contained an unknown level of error. Nonetheless, because the angles involved were so minute we made the following approximation, $\sin(\alpha) \approx \alpha$. This allowed a negligible baseline distance measurement error and therefore usable as the base distance in all of the trigonometric calculations.

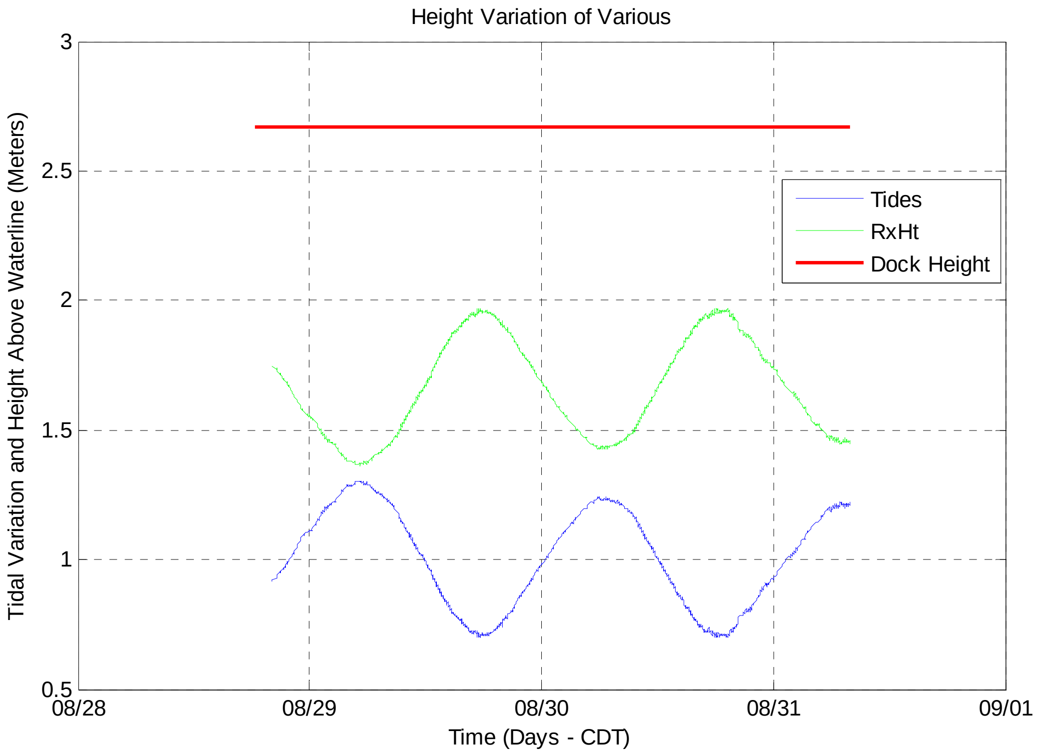

Figure 28. Mean sea level height plot of tides, Rx antenna and stationary dock.

First, a benchmark slant path distance between the RF equipment was attained by way of the Pythagorean Theorem, and modified by the changing height above water due to tides (as depicted in Figure 28). Not surprisingly, the path lengths, when plotted over time, were unremarkably similar in nature to the base tidal fluctuation, though 180° out of phase. This phase issue arises from the simple logic that low tide correlates to the highest antenna height and vice versa for high tide.

Next, these direct path lengths were compared to the single bounce-path lengths, which were calculated using Snell's Law (angle of incidence equals the angle of reflection). Based on the assumption that the strongest portion of the waveform would scatter at this approximate midpoint of the waterline separation distance, the total bounce path ray length was simply the hypotenuse of the mirror image triangle formed by the aforementioned law. Thus, total bounce-path length was:

$$\text{BouncePath (BP)} = \sqrt{BL^2 + (RxHt + TxHt)^2} \tag{17}$$

where *BL* is the baseline path length (waterline), and *RxHt* & *TxHt* are the heights of receiver and transmitter respectively.

Understandably, these results were also sinusoidal in nature but when plotted against the standard 1 Hz time-series, the mean vertical height displacement was only 1.685 cm and the maximum path length difference between the two was 1.64 cm (Figure 29).

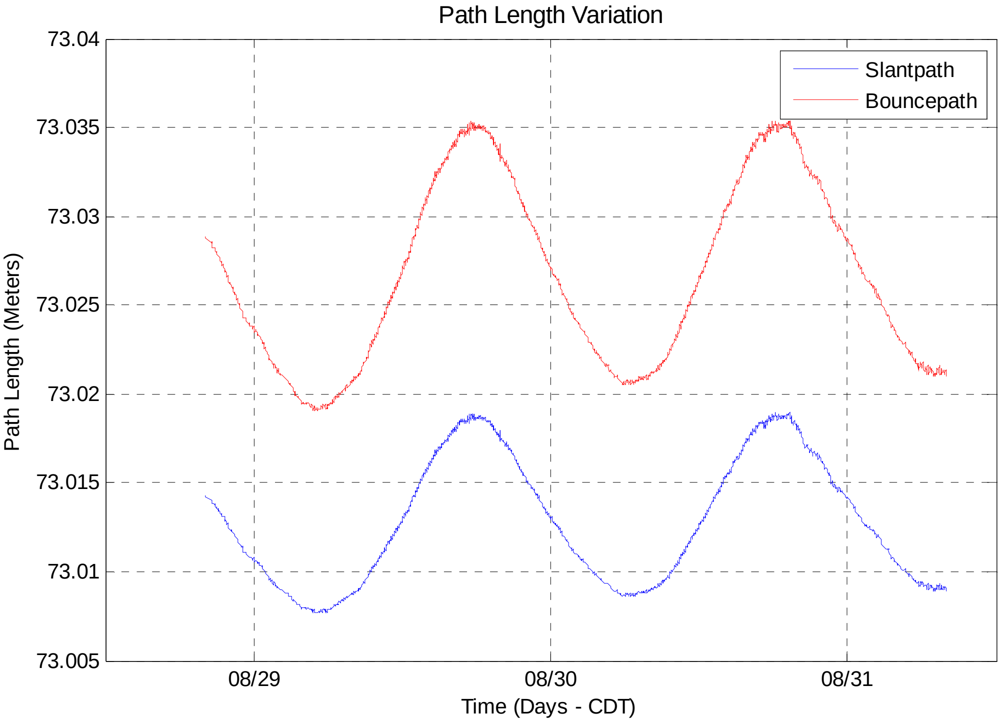

Figure 29. Direct (slant) path to surface scattered ray path length.

Given our 1.78 GHz operating frequency, which corresponds to a wavelength (λ) of 16.85 cm, the oscillations in RF net loss could not be due to complex sub-beamwidth interactions of antennae lobe patterns. This is because the direct ray path distance was very small, the target receiver did not move, and the transmit antennae's beam shape was uniform for all observed parts of the antenna pattern (3dB drop off was 40˚). Additionally, in 1997, Fabry et al. conducted a similar study using S-band microwaves (≈3.0 GHz) that lends credence to the above assumptions. In particular, he found that in cases of fixed, point-like targets, the phase of the target was relatively insensitive to sub-beamwidth inaccuracy in antennae pointing (as opposed to complex interference of antennae lobe patterns), but very sensitive to small path length differences.

Nonetheless, what Fabry and our results do depict is that even with very slight path length differences, significant phase difference variation results (Figure 30).

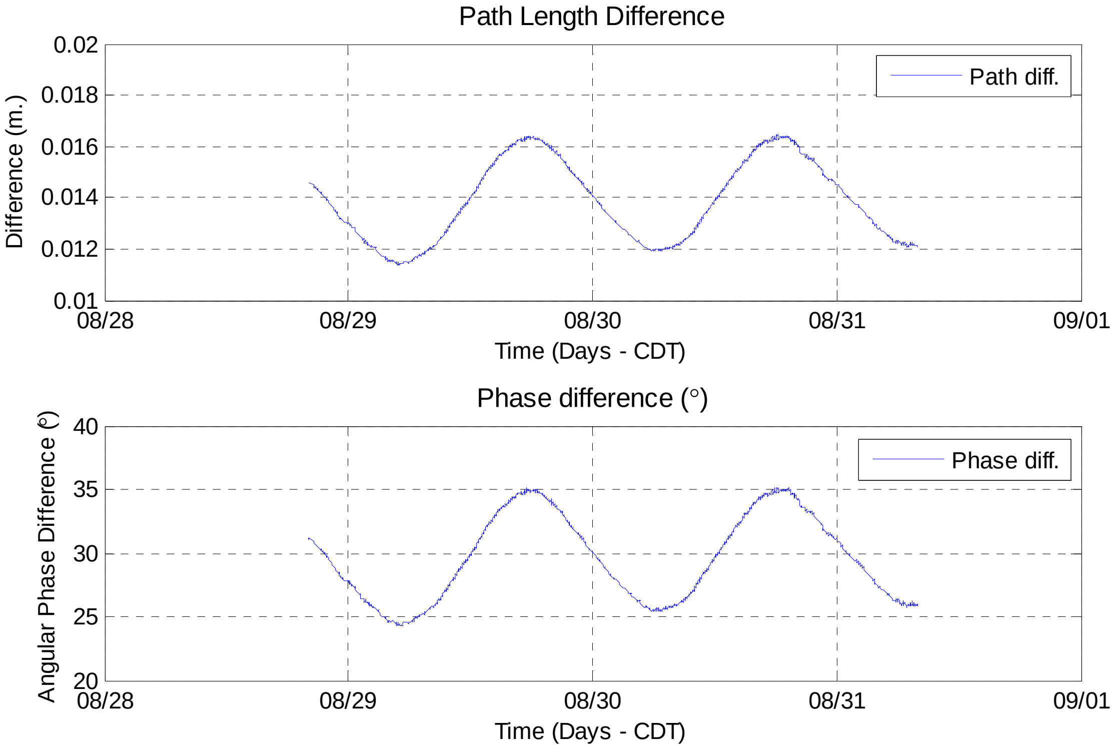

Figure 30. Path length difference (top) corresponding to phase difference (below) at 1.78 GHz.

Figure 31 is provided to illustrate the magnitude of interaction between two identical but phase shifted waves. Each sub-plot is composed of two generic sine waves of frequency 1.78 GHz, and unit amplitude. The top plot has been phase shifted by the minimum difference (24.31˚) as shown in Figure 30, while the second plot depicts the maximum (36.03°). Relative increase/decrease in amplitude of the resultant wave is provided in the text and clearly shows that minute angular differences, particularly when paired with the theoretical reflection coefficient of an ideal glossy surface ($R(\theta) = -1$), result in drastic changes in amplitude. In this case, the reflection coefficient accounts for the 180° phase shift incurred by the ray scattering off of the surface of the water.

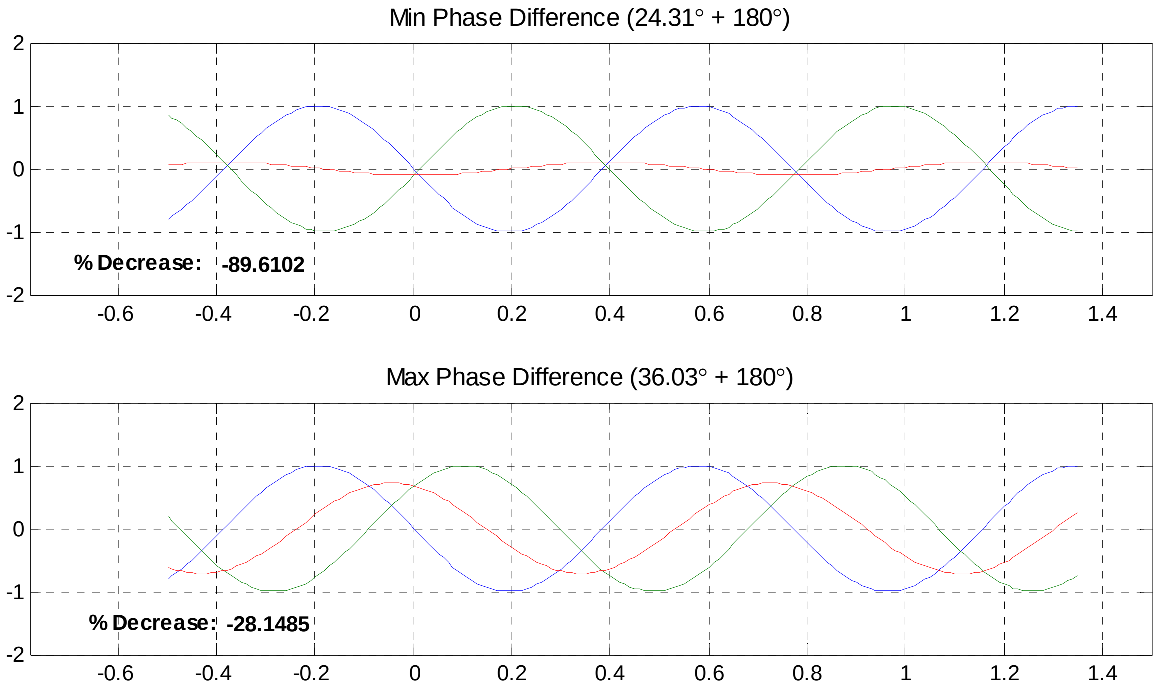
Min Phase Difference (24.31° + 180°)

Max Phase Difference (36.03° + 180°)

Figure 31. Illustration of destructive interference. Blue curve is zero phase, green is the phase shifted waveform, and red is the sum of the two.

Thus, in summary, when tidal height was at a maximum, antenna height was at a minimum, which resulted in minimal phase difference and therefore maximum destructive interference (as shown in Figure 32). Note as well the "inversion" of the RF Loss vector, which was calculated as P_{Rx}-P_{Tx}, as opposed to preceding versions. This provided the same information but presented in a manner more intuitive at this stage of the analysis.

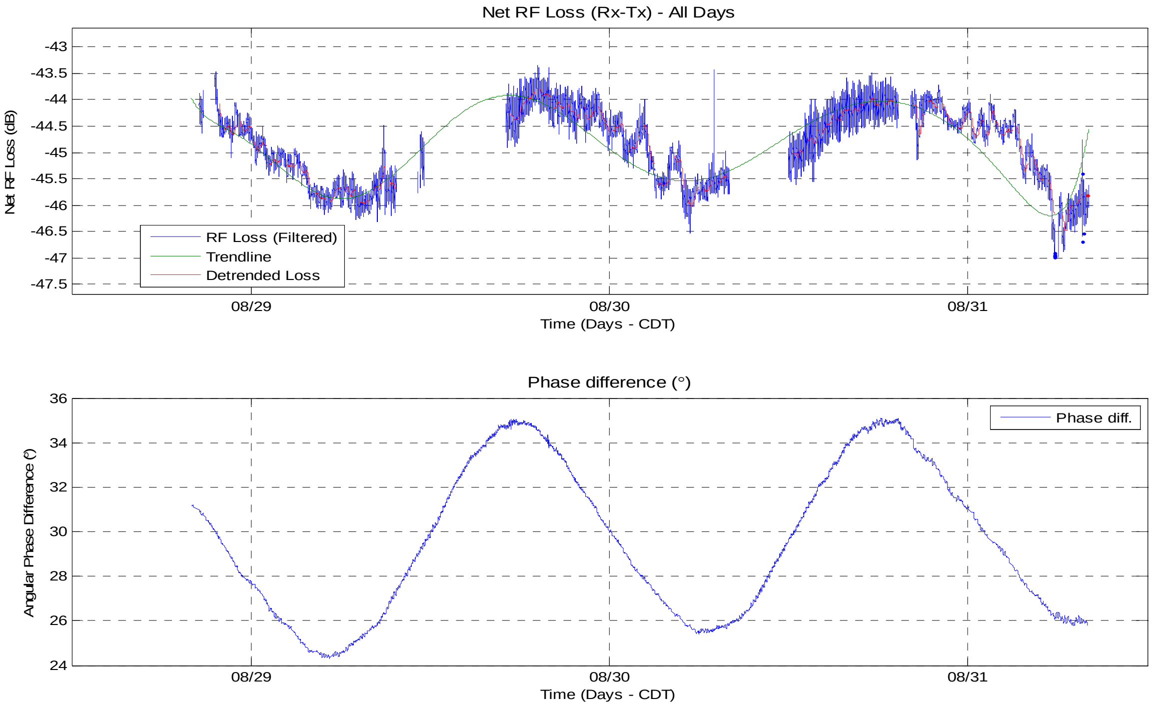

Figure 32. RF loss to phase difference time-series.

F. MODELED DATA COMPARISON

1. Introduction

The focus of most prior modeling and empirical propagation studies has been of ranges greater than 200 meters. There exists an extensive body of literature on long-range propagation at frequencies up to approximately 2 GHz. In 2004, Dr. W. M. Merrill and his cohort extended this research to the RF ground wave by considering lower antenna heights and shorter ranges for a variety of outdoor locations. This study capitalized on his empirical and modeled results by first confirming his low elevation data subset findings, and then broadening the scope to include the ranges associated with the NEP-6 experiment.

2. Theory

The propagation of an RF signal is governed by Maxwell’s Equations. The electric field near the surface is given by the solutions to (Wait, 1998)

$$E = -\frac{1}{kn^2} \nabla \times \nabla \times U_r \, , \tag{18}$$

where k is wave number, n is index of refraction and Ur is the electric field. Traditionally, the far-field (Fraunhofer) zone is simply described as that region of radius r, in which $r >> \lambda$. For the operating frequency used, λ=16.85 cm, which places the receiver well within the far-field. In this region, the solution to the above second order partial differential equation is the following plane wave:

$$E = E_0 \frac{e^{ikr}}{kr} \, , \tag{19}$$

where E_0 is a constant, r is the direct path ray and k is wave number. In this development, we shall only consider the case of a transmitter and receiver operating near the surface of a perfect reflector (see Figure 33). Following the standard plane wave combination, the electric field at the receiver is:

$$E = E_0 \frac{e^{ikr}}{kr} + R(\theta) E_0 \frac{e^{iks}}{ks} \, , \tag{20}$$

where r is the direct path and s is the reflected path. For grazing angles near zero $(\theta \,\square\, 0)$, the reflection coefficient, $R(\theta) = -1$, which is consistent with an ideal lossy surface. Taking advantage of the symmetry afforded by Snell's Law, the path length is determined by the direct path ray and the respective heights of transmitter (h_1) and receiver (h_2):

$$s = \sqrt{r^2 + (h_1 + h_2)^2} \, . \tag{21}$$

Henceforth we will refer to the total height, h=h_1+h_2. Near the surface, r is much greater than h and thus Equation (21) can be represented as a binomial series expansion, here to the fourth order (Stewart, 2008):

$$s \approx r \left[1 + \frac{1}{2}\left(\frac{h}{r}\right)^2 - \frac{1}{8}\left(\frac{h}{r}\right)^4 \right], \tag{22}$$

or for the inverse, since that will be needed later:

$$\frac{1}{s}=\frac{1}{r}\left[1-\frac{1}{2}\left(\frac{h}{r}\right)^2+\frac{3}{8}\left(\frac{h}{r}\right)^4\right]. \tag{23}$$

The expansion of the exponential is bit more complicated. From Equation (20), we utilize a Taylor series expansion of the reflected signal s about the direct path r,

$$\begin{aligned} e^{iks} &= e^{ikr}e^{ik\left[\frac{1}{2}\left(\frac{h}{r}\right)^2-\frac{1}{8}\left(\frac{h}{r}\right)^4\right]} \\ &\approx e^{ikr}\left[1+\frac{ik}{2}\left(\frac{h}{r}\right)^2+\frac{ik(k-1)}{8}\left(\frac{h}{r}\right)^4\right] \end{aligned} \tag{24}$$

The effective field is the sum of the direct and reflected fields, as follows:

$$\begin{aligned} E &= E_{dir}+RE_{ref} \\ &\approx \frac{e^{ikr}}{kr}\left[\left(\frac{h}{r}\right)^2\frac{ik-1}{2}+\left(\frac{h}{r}\right)^4\left(\frac{3}{8}+ik(k-3)\right)+\left(\frac{h}{r}\right)^6\frac{ik}{16}(4-k)\right] \end{aligned} \tag{25}$$

Since power is simply the electric field times its conjugate (after neglecting 5th order terms and higher), we find the power difference between the direct signal and the reflected signal to be,

$$\begin{aligned} P &= E\times E^{*} \\ &= \frac{1-k^2}{4k^2r^2}\left(\frac{h}{r}\right)^4, \end{aligned} \tag{26}$$

rather, a fourth-power drop off with height (Goroch, personal correspondence, 2010).

At frequencies from 900 MHz to 5.8 GHz, the dominant propagation effects can be modeled well with ray-tracing analogies, a mindset well suited to the analysis of our data. Due to the protected nature of the harbor in which this experiment was conducted, contributions from surface roughness scattering or lateral waves at the vegetation interface along the water's edge were not considered substantial. As expected due to the above derivation, and similar to Merrill's (2004) findings, near a finite-conductivity surface, a fourth-power propagation falloff with height above the scattering surface was empirically observed, although unlike Merrill, this study utilized only vertical polarization.

This falloff can also be explained pictorially by way of a ray-tracing analogy in which destructive interference between the direct-path ray and surface bounce ray resulted in varying degrees of received signal strength (See Figure 33).

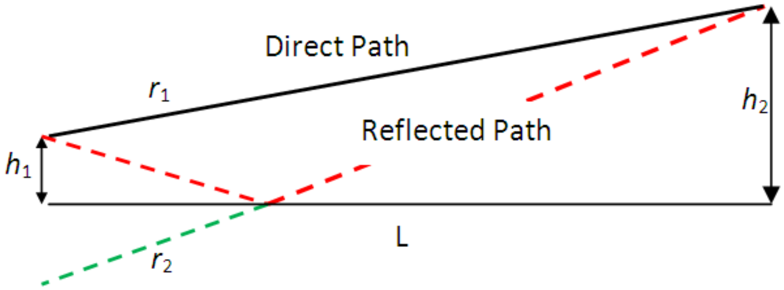

Figure 33. Direct path ray and reflected path actual (in red) and virtual (in green) rays.

Merrill’s simple two-ray model, as presented in Equation (20), provided the basis equations for modeling the expected RF Loss in our particular environment. However, because this study did not observe significant surface roughness, nor was it measured empirically, Equation (20) can be simplified to Equation (27). This generalization also takes into account the expansion of Equation (20) for circumstances in which the ratio of antenna height to path distance is very small, rather $^{h}/_{r}$ □ 1.

The following frequency/polarization-independent form of Equation (27), was used in the modeling portion of this experiment (Merrill et al., 2004, p. 38):

$$\frac{P_{Rx}}{P_{Tx}} = \left(\frac{h_r h_t}{r^2}\right)^2 . \tag{27}$$

where:
P_{Rx} = Received power (dBm)
P_{Tx} = Transmitted power (dBm)
h_r = height of receiver (m.)
h_t = height of transmitter (m.)
r = ray path-length (m.)

Excepting a few scaling constants, Equation (27) is identical to the derived Equation (26). They are both included to depict the linkage between the theory behind RF propagation and practical application of said formula.

3. Model Summary

Merrill's investigation of propagation loss in his *Quantifying Short-Range Surface-to-Surface Communications Links* (2004) made use of multiple *discrete* antenna heights and path lengths to build an empirical data set, yet his modeled data set varied continuously. The NEP-6 experiment is notable in that we took advantage of the continuously varying antenna height as a function of tides, thereby yielding a much larger empirical data set. This novel approach provided a continuous change of the antenna height which would be more difficult to accomplish over land. Modeled data were calculated via Equation (27) and sub-plotted against actual net RF loss. This plot clearly depicted the aforementioned height dependency in both versions of the net loss data set. Furthermore, after properly scaling the modeled data, these two vectors were then overlaid on the same axis (Figure 34).

Scaling was accomplished by first multiplying the modeled loss by the mean of the *actual* RF loss vector, and then dividing the mean of the *modeled* RF loss vector. This provided the fourth power drop-off in both empirical and modeled data in the overlay plot.

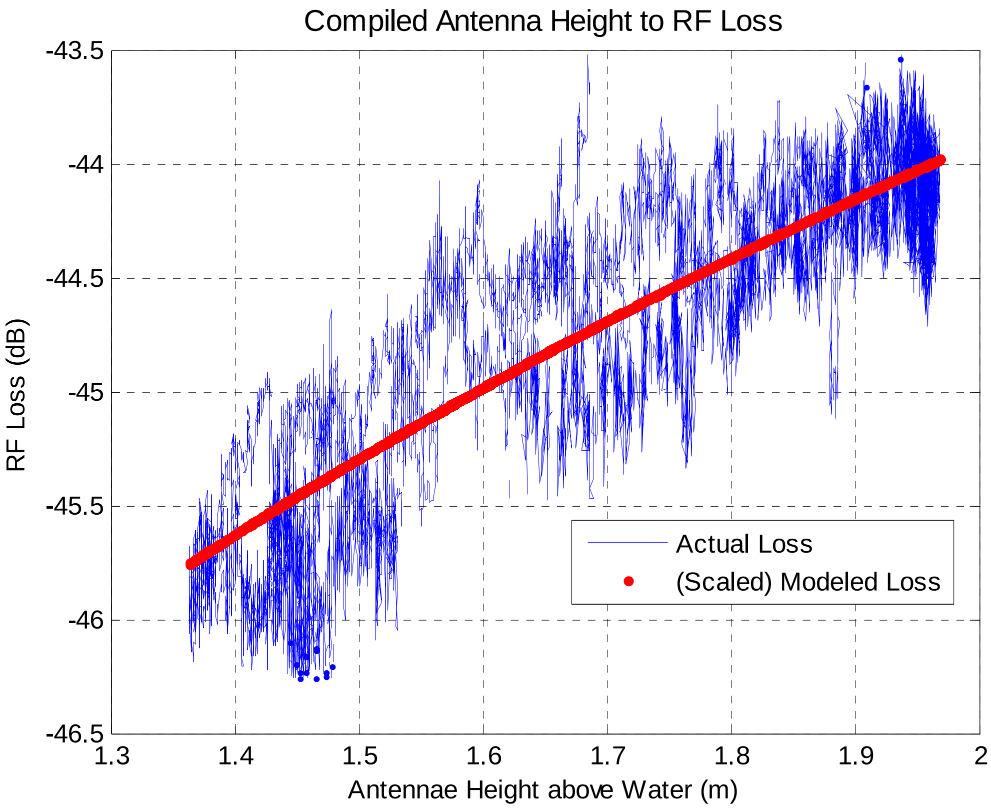

Figure 34. Empirical and modeled (scaled) RF loss (See Equation 27) to antenna height.

From theory, we have mathematically shown that the net propagation loss of the 1.78 GHz wave depends on the height of the antenna above the water surface. As illustrated in Figure 34, the near-surface empirical and modeled data exhibit the very same behavior of waveforms from much higher up in the atmosphere, which is correctly described by classic wave propagation equations. Additionally, the calculated RSSI of the modeled waveform portrays this same tendency, particularly with respect to tidal variation and path length difference (Figure 35).

In summary, the overall result is a definite dependency of propagation loss to antenna height in both the real-world data, as well as the modeled data.

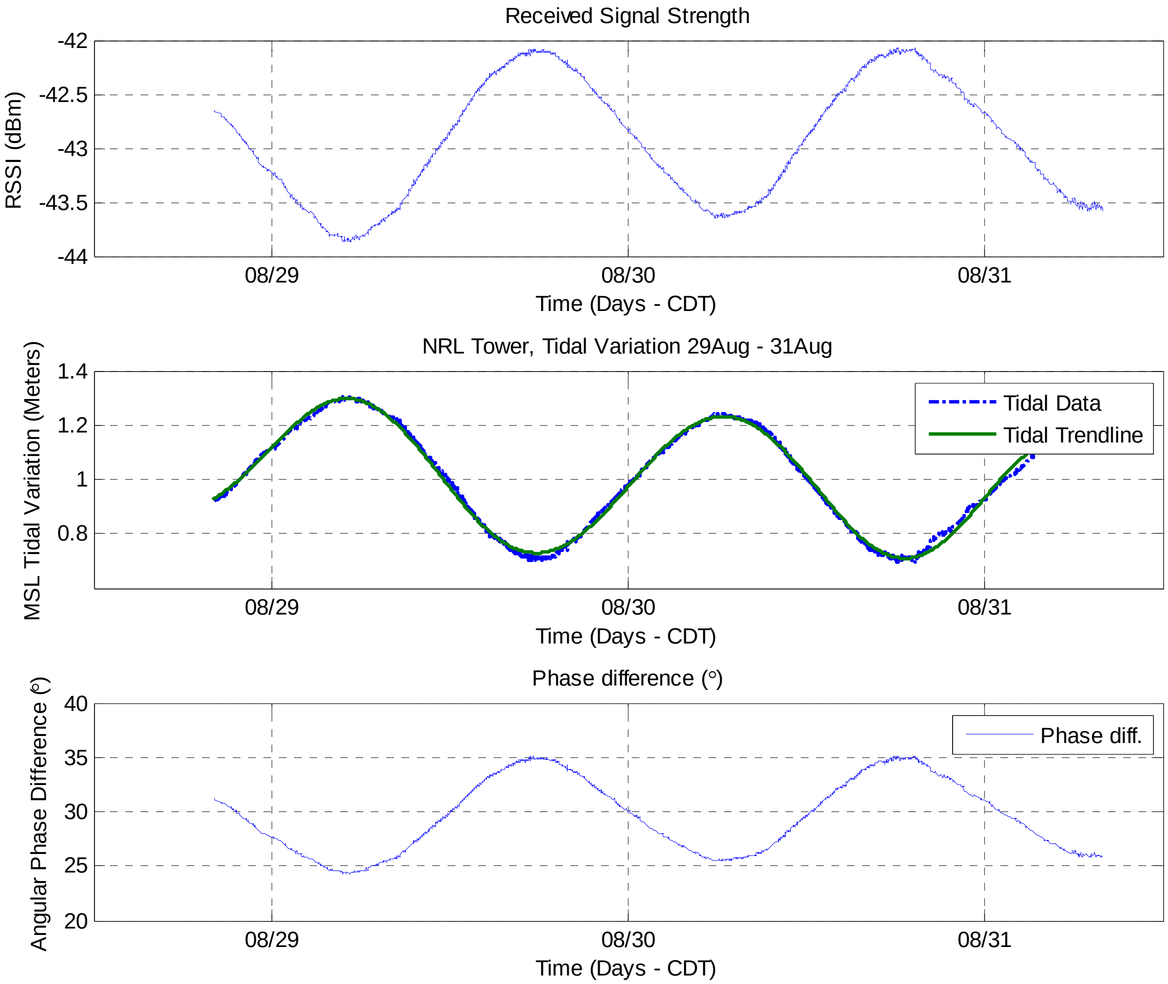

Figure 35. Modeled RSSI characteristics.

THIS PAGE INTENTIONALLY LEFT BLANK

V. CONCLUSION

A. SUMMARY OF EXPERIMENT

In this study, a 1.78 GHz waveform was emitted at a very low altitude over a protected body of water and the received signal power was measured. Additionally, various meteorological and oceanographic variables were sensed and preserved in a self-contained wireless data logging network. These data were then used to first calculate net propagation loss of the RF wave, and then in subsequent iterations, to correlate potential cause of the loss to the measured environmental parameters.

B. KEY RESULTS AND CONCLUSIONS

While a certain number of the collected environmental variables did play a small role in the resultant cyclic behavior of the net loss vector (e.g., solar irradiance), the vast majority (i.e., temperature, humidity, and wind), were not correlated to RF propagation loss at a statistically valid level of significance. Tidal variation was the predominant environmental parameter to have an effect, and yet even this was merely the underlying cause for antenna height variation. In summary, the overall result of this experiment was that in the given near-surface environment, meteorological variance did not seem to have a concrete impact on propagation loss. Additionally, we found that antenna height played a direct role in propagation loss; a result currently accepted in EM/EO waveform propagation theory, and one that we discovered to still be pertinent in the near surface environment for the test range used. Finally, these results were confirmed both mathematically and via modeling using appropriate propagation loss calculations.

C. APPLICABILITY TO DOD OPERATIONS

It is certainly accepted that the exploitation of unmanned and autonomous vehicles, regardless of the medium in which they are used, can only increase in future DoD operations. However, with their application come certain limitations and constraints, most notably the need for reliable communication. While this experiment explored a very narrow subset of potential operating conditions, it still provides valuable insight as to the expected behavior of these systems.

Many U.S. forces utilize RF and optical propagation programs, such as AREPS and TAWS, to predict waveform behavior in a given mission environment. These programs are excellent provided the user does not require predicted waveform behavior near the surface or transmitting antennae, where the model quickly falls apart. With the inclusion of these remarkably simple yet pertinent results, the area of coverage of the above propagation models could be extended to include the near-surface. This is critical to today's militaries that operate complex systems using RF energy in this near Earth environment.

Maritime security, particularly that portion related to harbor security, is a rapidly growing field that has spawned numerous commercial and governmental agencies dedicated to defeating the threats pervasive in this complex environment. The use of unmanned surface and undersea vehicles could revolutionize this industry by reducing the workload as well as removing personnel from dangerous areas. Additional avenues might also include simple security networks comprised of video, audio and other pertinent environmentally sensed values (air temperature, humidity, wind speed, etc.) that would be transmitted via EM energy to a central repository. However, to make this realizable, communication and control must be assured. From this research, we find that much of this problem could likely be solved by sufficient power output and placement of the transmitting antenna.

Finally, this question of command and control naturally extends into overland and aerial vehicles, with much headway being made in the mid- and long-range arenas. However, by their very nature, these vehicles operate at much higher altitudes where sufficient antenna height is assured. For very short range, or very low altitude/cluttered environment scenarios, the results of this experiment can certainly be applied.

D. AREAS FOR FURTHER RESEARCH

Classic theory dictates that RF wave propagation above the surface layer is dependent on antenna height. While this study has clearly shown that this characteristic extends into the very near surface environment, it does so only at a given frequency and path distance. Merrill et al. produced similar results over a variety of path lengths, frequencies and environments, but with much fewer data points per trial. In order to make valid generalizations of this RF propagation phenomenon, it is necessary to duplicate the above experiment but over a much longer time frame, with a wider range of environmental conditions, and over a wider set of operating frequencies and antenna heights.

Additional analysis of the current data set would also be beneficial as this study only reviewed the 1.78 GHz frequency set. It would be interesting to see if the same results were obtained from the 225 MHz data and if so, the magnitude of difference between the two. Dr. Christopher Anderson of the United States Naval Academy conducted a similar propagation experiment concurrent with NEP-6 that was driven by different goals. Nonetheless, the data that he collected could be useful when compared to the current data set.

All of the above recommendations lead to ultimately establishing a generalization of RF propagation in the near surface environment. Once this has been completed, it then becomes necessary to include these results in both current (i.e., AREPS) and future wave propagation models, thereby improving our ability to predict RF wave behavior and thus expand the reliability and security of remotely controlled unmanned vehicles, and wireless security networks.

THIS PAGE INTENTIONALLY LEFT BLANK

APPENDIX

A. SUPPLEMENTARY BACKGROUND INFORMATION

1. Atmospheric Boundary Layer

The atmospheric boundary layer (ABL) is the part of the troposphere that is directly influenced by the presence of the Earth's surface and responds to surface forcing with a time scale of about one hour or less. Over the oceans, the boundary layer depth typically varies slowly in space and time. Under certain conditions, such as on a clear calm day, diurnal variations in sea surface temperature may be observed because of the solar insolation and little wind-generated turbulent mixing in the upper ocean. However, such diurnal variation is much weaker in comparison to that in the atmospheric boundary layer. Thus, temporal variation in surface thermal forcing is predominantly a result of atmospheric temperature variability. Other sources of surface forcing in the atmospheric boundary layer include frictional drag, evaporation and transpiration, heat transfer, pollutant emission (in case of scalar concentrations), and terrain (or surface water wave) induced flow modifications. These sources of forcing both directly and indirectly affect EM wave propagation via changes in the index of refraction and surface reflections due to turbulence (surface roughness) and turbulent fluxes (Stull, 1988).

As shown by Stull (1988), there are multiple layers to the ABL, but for the purposes of this experiment, we will be focusing on the *surface layer*. This layer is comprised of the lowermost 10% of the ABL in which the log wind profile is valid. Vertical variations of the mean wind and temperature (i.e., mean profiles), are determined by the structure of the roughness elements (in this case, waves, sea sprays, and swells).

2. Turbulence and Flux

Turbulence, which is the mechanism for mixing, is not a feature of fluids but of fluid flows. The governing equations for turbulent flow is the same in all fluids, whether they are liquids or gases and if the Reynolds number (the ratio of inertial force to viscous force) is large enough, the major characteristics of turbulent flows are not controlled by the molecular properties of the fluid in which the turbulence occurs. Turbulence is one of the principal unsolved problems in physics today due to its nonlinear and random nature. Since the Navier-Stokes equations of motion are nonlinear and a deterministic solution has yet to be found, each individual flow pattern has certain unique characteristics associated with its initial and boundary conditions. Thus, while frustrating and currently incomplete, the study of turbulence has led to the following basic properties: irregular, diffusive, three-dimensional vorticity fluctuations, and dissipative (Stull, 1988).

If turbulence is a feature of a mixing flow, eddies are the vehicle by which it occurs. The largest are called energy containing eddies and are typically the depth of the boundary layer in an unstable atmosphere. In a stable atmosphere, energy-containing eddies are defined by the vertical distance of the ABL from the surface. These large eddies deform and stretch, thereby creating smaller eddies, and so on to the smallest turbulent eddies characterized by the Kolmogorov microscale, η (See Equation 28). Eddies smaller than η are called dissipation eddies, where turbulent kinetic energy is dissipated via molecular viscosity.

$$\eta = \left(\frac{\nu^3}{\varepsilon} \right)^{1/4} \tag{28}$$

where η: size of the smallest eddy
ν: viscosity (m^2/s)
ε: dissipation rate (m^2/s^3)

Flux, in all its various forms, is particularly important when discussing the effects of turbulence on its environment. There are many methods for diagnosing flux, but all make use of Taylor's Hypothesis (that turbulent eddies are frozen in time) and most are dependent on the stability of the atmosphere. In neutral stability conditions, the flux profile takes the following gradient relationship:

$$\frac{\partial \overline{u}}{\partial z} = \frac{u_*}{\kappa z} \tag{29}$$

where $\frac{\partial \overline{u}}{\partial z}$: shear
u_* : frictional velocity
κ : von Karman's constant
z : height or level

This relationship shows that the vertical shear of the mean wind, $\frac{\partial \overline{u}}{\partial z}$, is inversely proportional to height, *z*. In non-neutral conditions, the effects of a stability parameter must be considered as shown in the following:

$$\frac{\kappa\, z}{u_*}\frac{\partial \overline{u}}{\partial z} = \phi_m\,(\frac{z}{L}) \tag{30}$$

where $\phi_m\,(\frac{z}{L})$: momentum stability parameter (q, h are similar), although in the near surface, stability is typically not a factor as (z/L) is rapidly approaching zero.

This study will be utilizing the log wind profile for a neutral surface layer (no stability effects), with an important modification. It is possible to obtain frictional velocity, u_* directly from measurements, but this requires an accurate value for *roughness height*, z_0 (the base of the surface layer). Typically, this value is calculated via Charnock's Relationship over the water. Alternatively, in the surface layer, momentum flux can be obtained by taking measurements of mean wind (likewise for moisture, q_* , and heat, h_*) at two levels and make use of the following integrated flux profile relationship for neutral conditions.

$$u_* = \kappa\frac{\overline{u}(z_2) - \overline{u}(z_1)}{\ln\left(\frac{z_2}{z_1}\right)} \tag{31}$$

where z_1 and z_2 are the respective measurement levels.

B. SCATTER PLOTS OF RESIDUALS

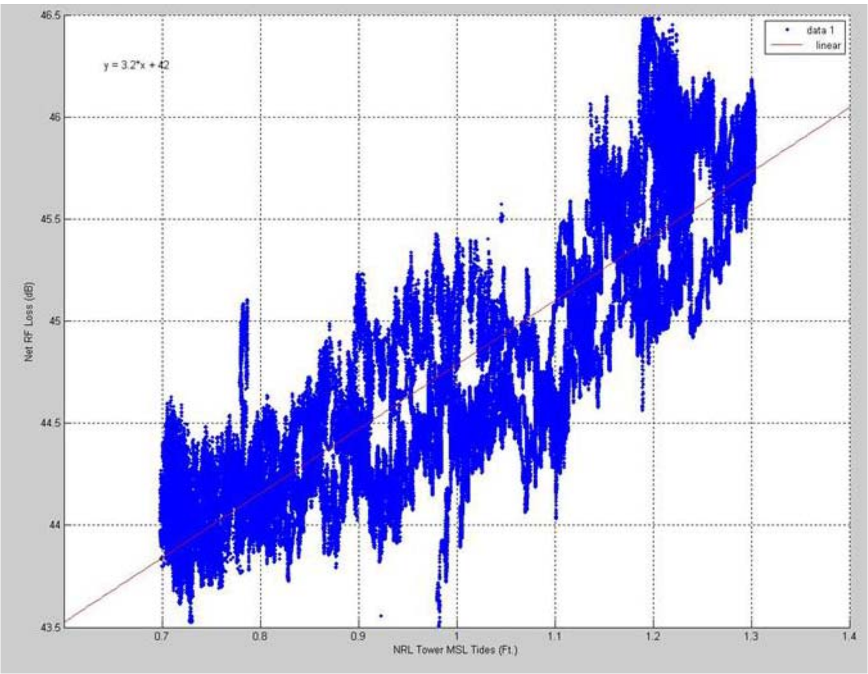

Figure 36. Scatter plot of tidal height to net RF loss (dB) in blue and linear trend-line (gray). All subsequent plot plots utilize the residuals from this calculation.

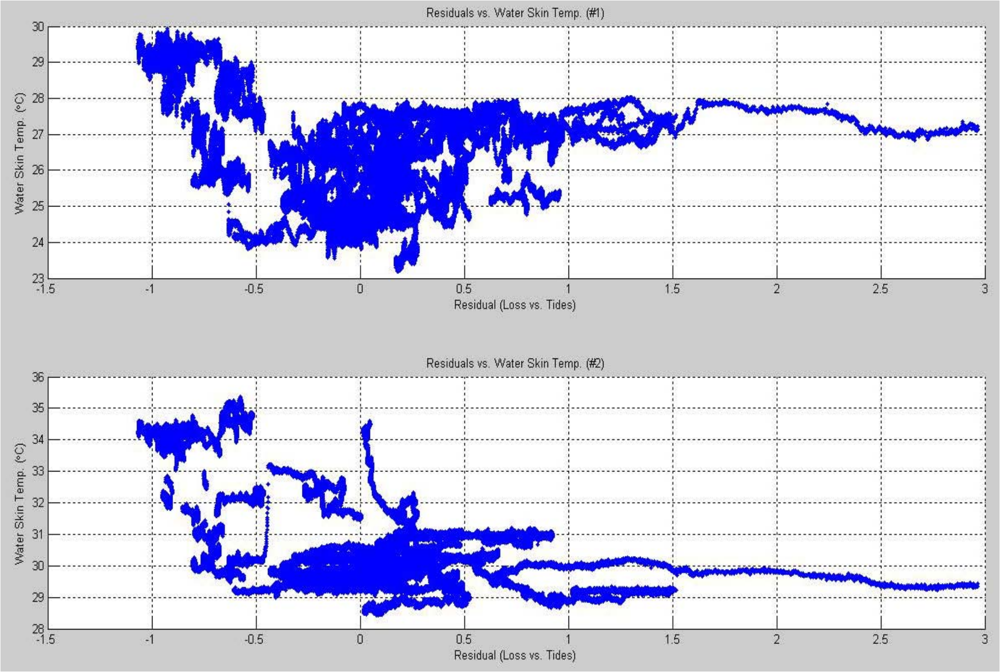

Figure 37. Scatter plot of calculated residuals to water surface skin temperature (˚C). The top plot is from sensor #KT18.85-I, the bottom from sensor #KT18.85-II.

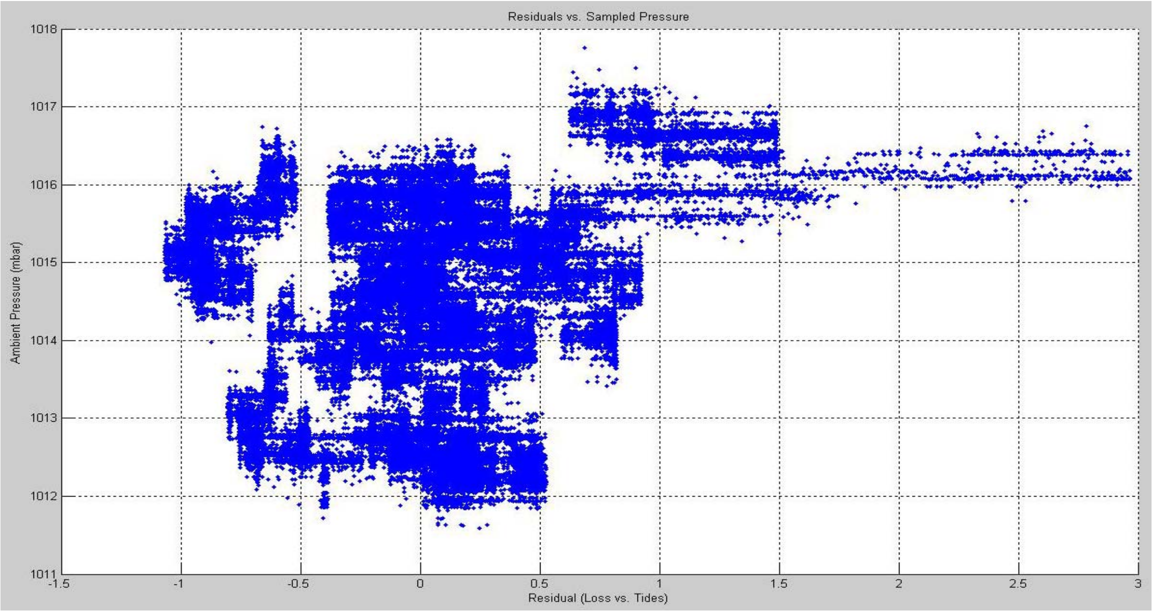

Figure 38. Scatter plot of calculated residuals to sampled atmospheric pressure (mbar).

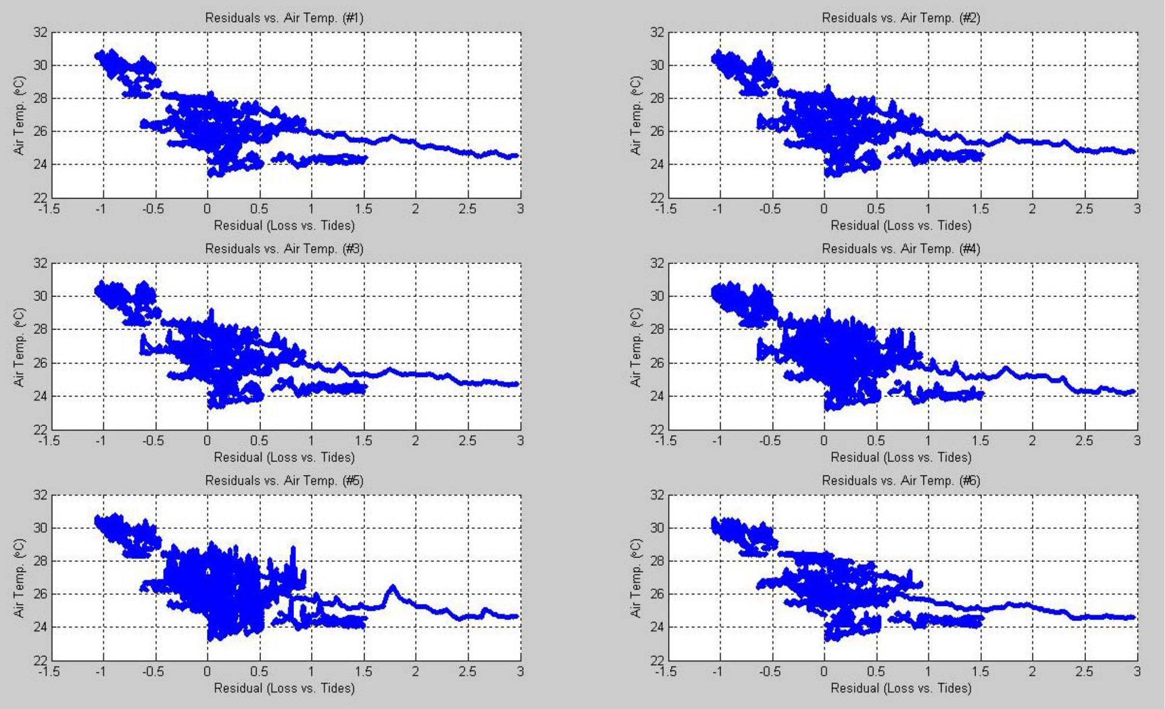

Figure 39. Scatter plot of residuals to air temperature (˚C) at each of the six levels.

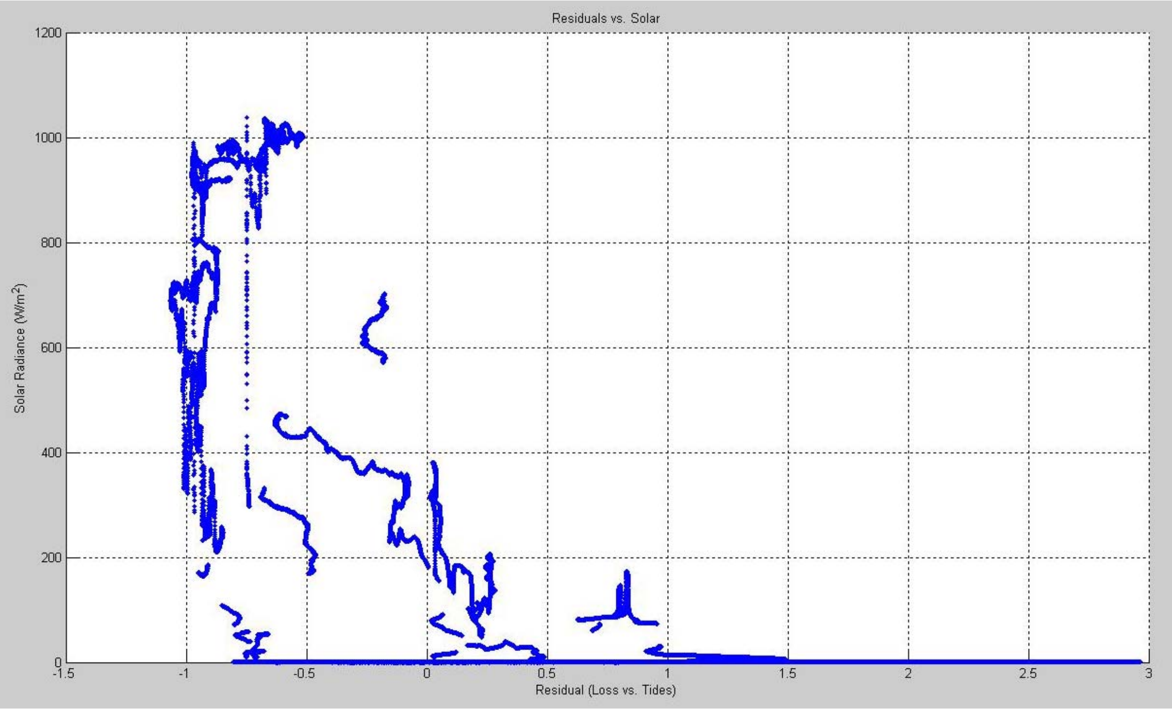

Figure 40. Scatter plot of residuals to solar irradiance (W m-2).

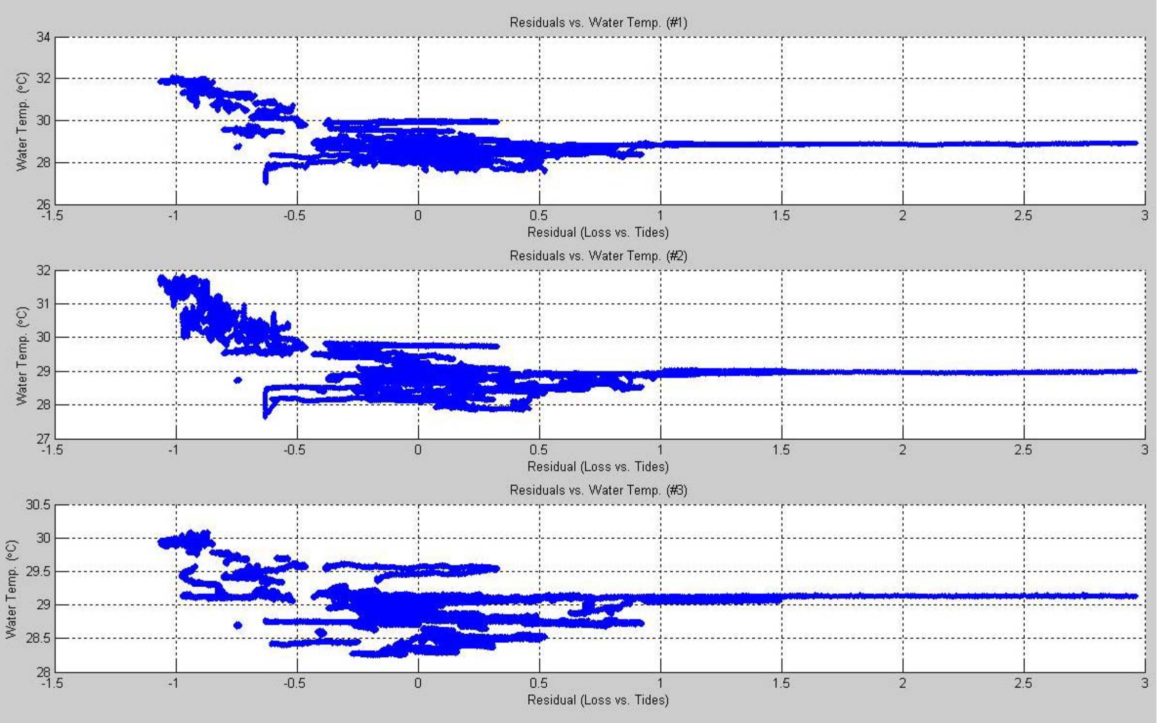

Figure 41. Scatter plot of calculated residuals to submerged water temperature (˚C) at each of the three levels, where #1 was 4.0 cm, #2 was 8.0 cm, and #3 was 18.0 cm below the surface.

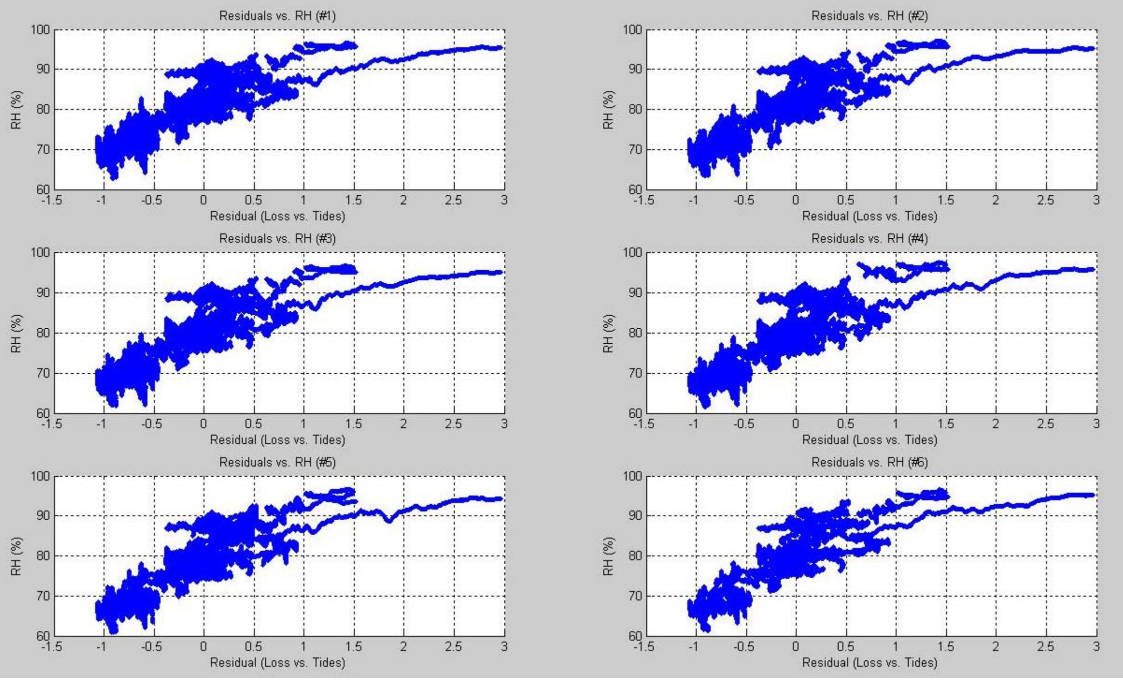

Figure 42. Scatter plot of calculated residuals to relative humidity (%) at each of the six measured levels. #1 was the lowest (11.5 cm), up to #6 which was the highest (247.0 cm) above the water surface.

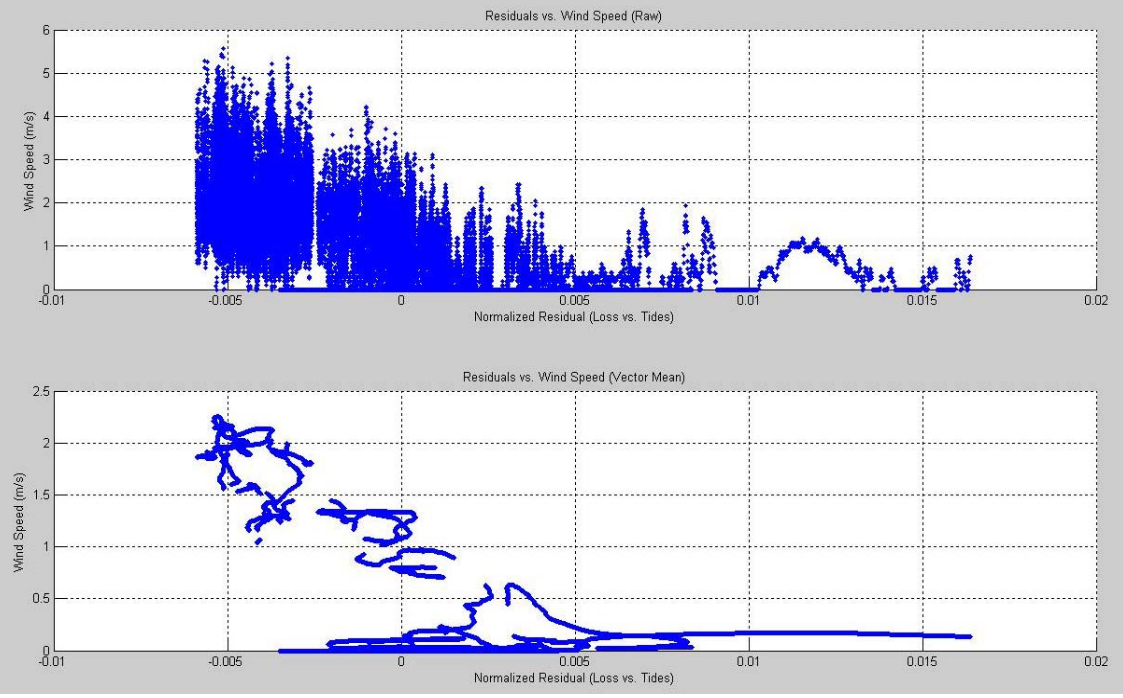

Figure 43. Scatter plot of calculated, normalized residuals to raw wind speed (top) and the vector mean of wind speed (bottom). Both plots are in units of m s-1.

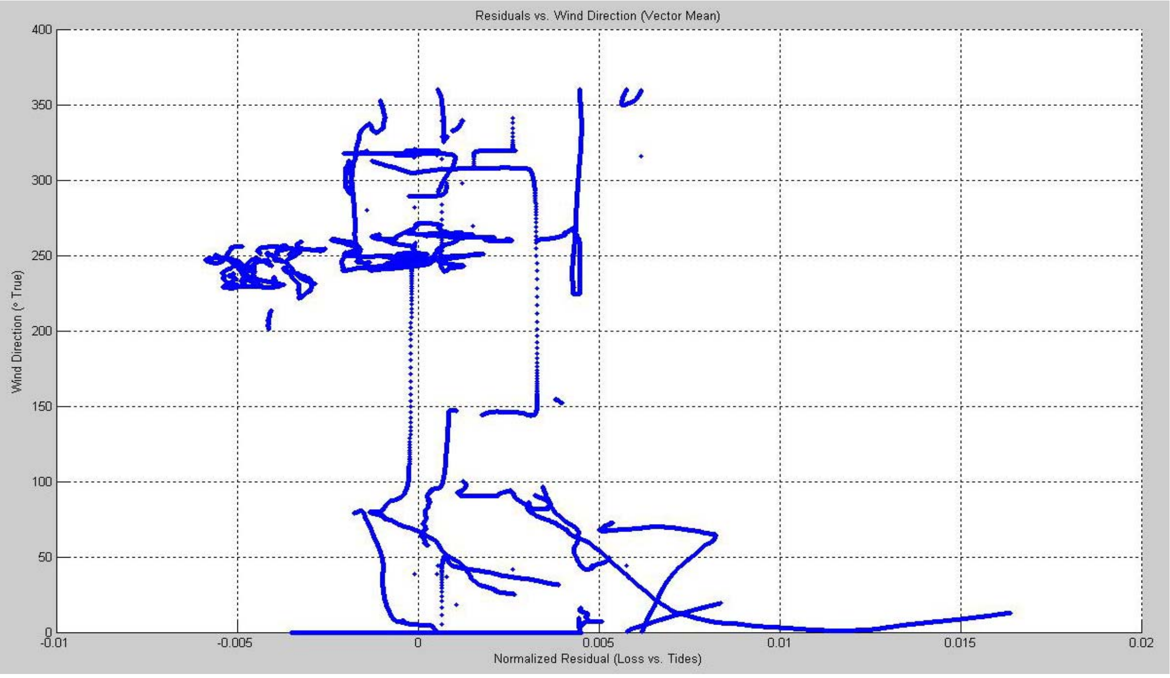

Figure 44. Scatter plot of normalized residuals to the vector mean of wind direction (˚True)

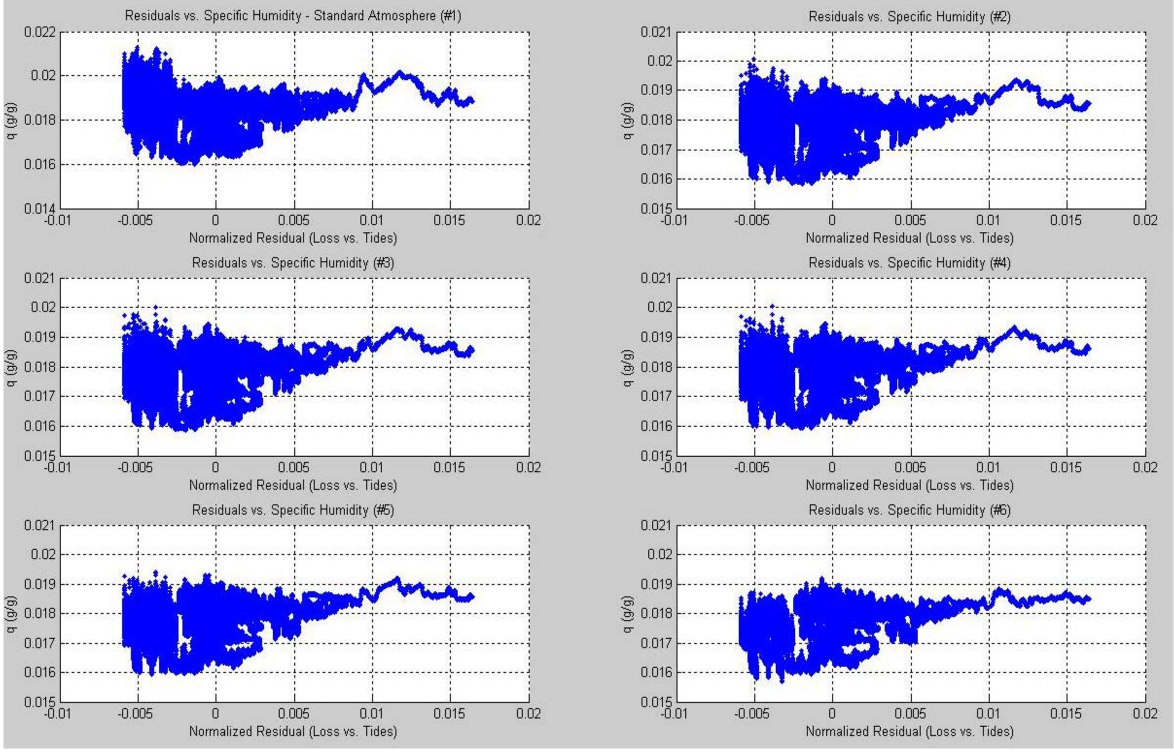

Figure 45. Scatter plot of calculated, normalized residuals to specific humidity (g g-1), at each of the six levels, and referenced to standard atmosphere (1013.25 mbar)

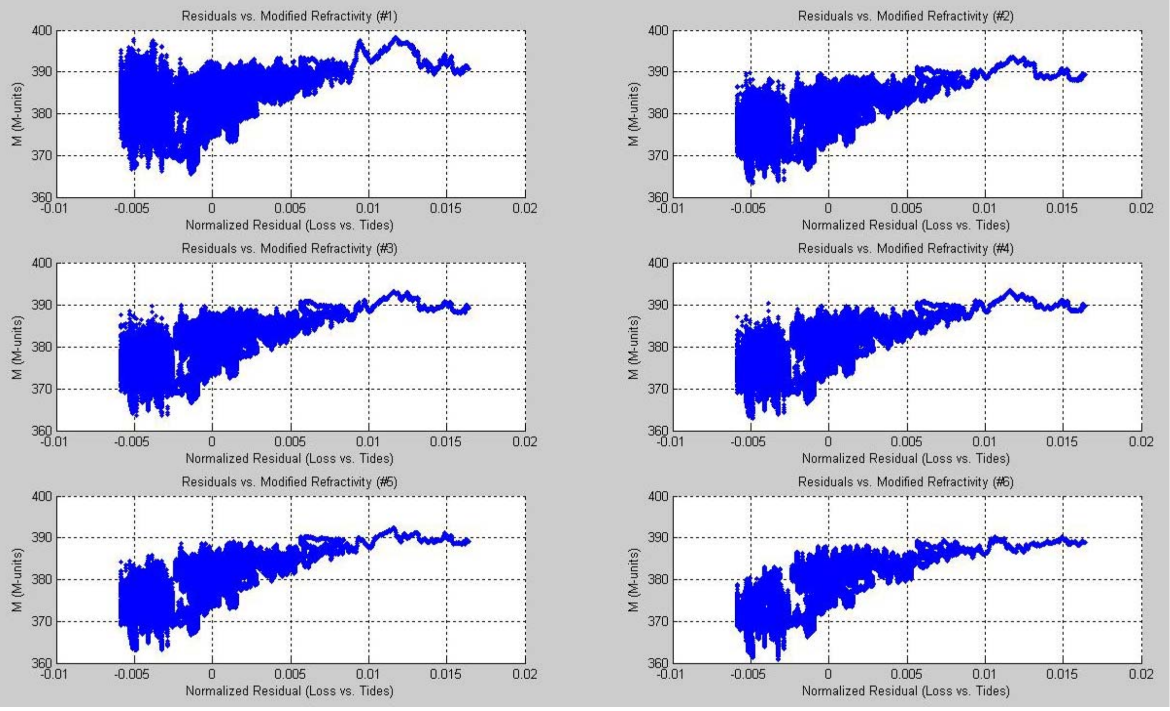

Figure 46. Scatter plot of normalized residuals to calculated modified refractivity (M-units), at each of the six observed levels.

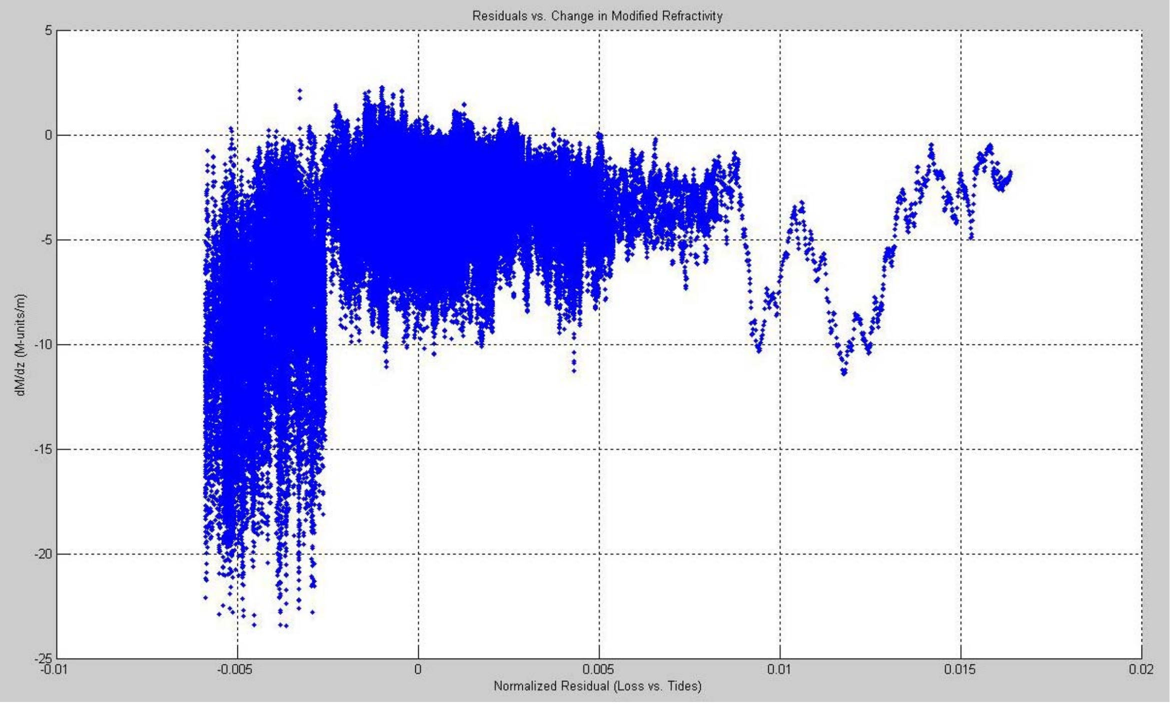

Figure 47. Scatter plot of calculated, normalized residuals to the gradient of modified refractivity (M-units m-1)

THIS PAGE INTENTIONALLY LEFT BLANK

LIST OF REFERENCES

Bean, B. R., and E. J. Dutton, 1968: *Radio Meteorology*, Dover Publications, Inc., New York, 435 pp.

Campbell Scientific, SR50A Sonic Ranging Sensor Data Sheet, 2009.

Cohen, J., 1988: *Statistical Power Analysis for the Behavioral Sciences*, Lawrence Erlbaum Associates, New Jersey, 567 pp.

SPAWAR Systems Center, 2007: *Refractivity Classes*. Space and Naval Warfare Systems Center, Atmospheric Propagation Branch, 2858, San Diego, CA. pp. various.

Fabry, F., Frush, C., Zawadzki, I., and Kilambi, A., 1997: On the extraction of near-surface index of refraction using radar phase measurements from ground targets. *Journal of Atmospheric and Oceanic Technology*, **14**, 4, 978–987.

Federal Standard 1037C. *Telecommunications: Glossary of Telecommunication Terms*, August 1996. [Available at: http://www.its.bldrdoc.gov/fs-1037/] Accessed September 2009.

Helvey, R. A., and J. S. Rosenthal, 1983: "Guide for Inferring Refractive Conditions from Synoptic Parameters," Technical Report, Pacific Missile Test Center, 36 pp.

Guildline Instruments Limited, AutoSal Data Sheet, 2002. [Available at: http://www.bodc.ac.uk/data/documents/nodb/pdf/Buildline8400BDatasheet.pdf] Accessed January 2010.

Kidder, S. Q., and S. H. Vonder Haar, 1995: *Satellite Meteorology: An Introduction*, Academic Press, New York, 466 pp.

Medwin, H., 2005: *Sounds in the Sea: From Ocean Acoustics to Acoustical Oceanography*, Cambridge University Press, New York, 643 pp.

Merrill, W., Liu, H., Leong, J., Sohrabi, K., and Pottie, G., "Quantifying Short-Range Surface-to-Surface Communications Links," *IEEE Antennas and Propagation Magazine*, **46**, 3, June 2004, pp. 36–46.

Rinehart, R. E., 1997: *Radar for Meteorologists, 3rd Edition*, Rinehart Publications, Grand Forks, 418 pp.

Stewart, J. 2008: *Multivariable Calculus: Early Transcendentals*, Brooks/Cole Publishing Company, New York, 1185 pp.

Stull, R., 1988: *An Introduction to Boundary Layer Meteorology*, Kluwer Academic Publishers, Dordrecht, Netherlands, 667 pp.

Thayer, G. D., 1974: "An Improved Equation for the Radio Refractive Index of Air." *Radio Science*, Vol. 9, No. 10, pp. 803–807.

Wait, J. R., 1998: "The Ancient and Modern History of EM Ground-wave Propagation," *IEEE Antennas and Propagation Magazine*, **40**, pp. 7–24.

Wilcox, R. R., 2005: *Introduction to Robust Estimation and Hypothesis Testing*, Academic Press, New York, 588 pp.

Wong, V., "Overland PC Network Layout," Naval Research Laboratories, unpublished materials, Washington DC (2009)

INITIAL DISTRIBUTION LIST

1. Defense Technical Information Center
   Ft. Belvoir, Virginia

2. Dudley Knox Library
   Naval Postgraduate School
   Monterey, California

3. Dr. Peter Guest
   Naval Postgraduate School
   Monterey, California

4. Dr. Andreas Goroch
   Marine Meteorology Division
   Naval Research Laboratory
   Monterey, California

5. Mr. Robert Wert
   Tactical Electronics Warfare Division
   Naval Research Laboratory
   Washington, DC